# Chapter 3

# Numerical modeling of the SBRC approach

## 3.1 The approach

The SBRC approach has been successfully applied to real data several times. Because equations (2.6) and (2.28) were derived in a quasi-heuristical way, a quantitative approach is required to verify the SBRC inversion algorithms based on them. Numerical simulations of seismicity triggered by fluid-injections in boreholes are performed as follows.

To model the triggering of microseismicity numerically, the process of pore pressure perturbation in a medium with (statistically) distributed criticality is simulated. For the modeling, a Finite Element Method (FEM) is used to solve the time-dependent parabolic equation of diffusion for a 2D and 3D medium. The modeling software (FEMLAB) is implemented into the MATLAB® computing environment. It forms an interactive tool for modeling and solving scientific and engineering problems based on partial differential equations (PDE). Here, the parabolic differential equation of diffusion is represented in general form, intended especially for nonlinear an non-stationary problems as required in this case. For solving the PDE, the Finite Element Method (FEM) is applied. The program runs that method in conjunction with adaptive meshing and error control as well as with a variety of numerical solvers. In the case of convection and diffusion, it can be distinguished between convection-dominated and diffusion-dominated problems. As a rule of thumb, diffusion-dominated problems, such as the heat or diffusion equation required here, yield very stiff systems. These can be integrated efficiently by specialized implicit stiff solvers provided by the software. These solvers turn out to be efficient in our cases where the solution is smooth. A more detailed description of the mathematical and numerical foundation can be found in the reference manual of the software.

The modeling and analysis scheme is basically separated into five parts schematically shown in figure 3.1. For simplification, the modeling scheme is explained in 2D here.

The realization of the approach proposed is performed in 2D as well as in a 3D space. The single parts in detail are:

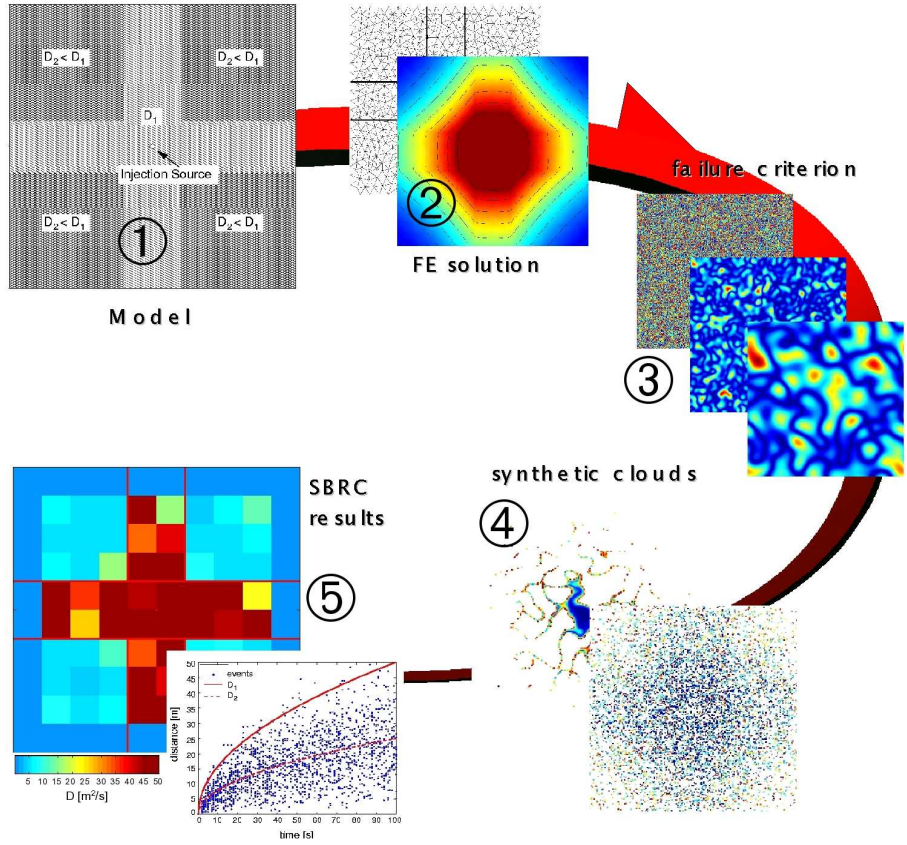


Figure 3.1: Scheme of numerical modeling. Based on FEM algorithms, the time-dependent equation of diffusion is solved for an arbitrary hydraulic model with simulated pressure perturbation. Comparing the solution with a statistically computed criticality, synthetic clouds of events can be obtained and analyzed using the SBRC inversion algorithms. In step 1, the set-up of the hydraulic model is shown. Colors denote hydraulic diffusivities used in the model. In step 2 the model is divided into a FEM grid where the solution of the diffusion equation is solved on (colors correspond to the pressure amplitudes). In step 3, the distribution of criticality is shown spatially uncorrelated and correlated using Gaussian autocorrelation functions. Colors correspond to the criticality value, blue colors denote unstable zones, red colors denote stable zones in the medium, respectively. Comparing steps 2 and 3, numerical microseismicity clouds are obtained when the pressure exceeds the criticality in a point of the medium (shown in step 4, colors correspond to the event occurrence time). In step 5, the analysis of the event clouds is performed in terms of the SBRC approach. Hydraulic diffusivity of the medium is estimated and reconstructed in 2D and 3D space (color correspond to the reconstructed diffusivities).

1. A hydraulic model with a pore pressure source located in the center is defined. As an input signal, a step-function-like pressure perturbation with amplitude $P_0$ is used. Generally, the position as well as the source function can be arbitrary and will be discussed later. The hydraulic diffusivity $D(x,y,z)$ of the medium can be distributed

homogeneously, heterogeneously (shown in figure 3.1), isotropic or anisotropic. Because the SBRC-method assumes a point source of pore pressure perturbation, the source in the modeling scheme is realized as a circle (in 2D) or sphere (in 3D) with a small radius compared to the size of the model. As it is shown later in the accuracy discussion, the source size is defined small enough to avoid boundary or source geometry effects. The overall size of the model is 200m $\times$200m ($\times$200m). The boundary conditions at the borders of the model are of Dirichlet type, i.e., fixing the pressure to zero there. The pore pressure amplitude at the source is also defined as a boundary condition in order to control the amplitude $A$ at the source.

2. The time-dependent parabolic equation of diffusion is solved using FEM algorithms. The spatio-temporal pressure distribution within the model $P_{fem}(x,y,z,t)$ is obtained on the irregularly spaced nodes of the finite element grid. In order to avoid boundary effects, only a part of size 100m $\times$100m ($\times$100m) is used for the analysis in the following. The pressure perturbation is modeled within the medium for a time of $t$=100 seconds with time increment of $\Delta t = 0.1$ or $\Delta t = 0.3$s. After obtaining the solution of the pressure perturbation the medium is divided into small regularly spaced cells. The solution $P_{fem}$ is interpolated on the regular grid without accuracy loss and the pore pressure distribution $P(x,y,z,t)$ is obtained. The size of the elementary cell is 0.46m$^2$ in 2D and 0.67m$^3$ in 3D, resulting in approximately 46000 and 3.3 millions cells, respectively.

3. Criticality (triggering criterion) $C(x,y,z)$ is defined. It is randomly distributed in the medium within a given range of pressure amplitude. This procedure directly follows the concept of the SBRC approach, that real rocks are in a critical state of stress in some places. By correlating the criterion spatially by using exponential or Gaussian autocorrelation functions, the influence of different types of criticality statistics can also be studied.

4. Synthetic clouds of events can be created by comparing $P$ (step 2) and $C$ (step 3) for each cell in the medium and time step: Triggering occurs at cells where the amplitude of pore pressure perturbation $P(x,y,z,t)$ exceeds the failure criterion $C(x,y,z)$. The so defined event is characterized by its position $x_e, y_e, z_e$ and occurrence time $t_e$. This procedure allows one to obtain synthetic clouds of events.

5. The event clouds are analyzed in terms of their spatio-temporal evolution character. By applying the SBRC algorithms as described in chapter (2), the hydraulic diffusivity is calculated. Scalar estimates of effective hydraulic diffusivity are obtained as well as the distribution of diffusivities in 2D/3D. They are compared with the input values of the model in step (1) to verify the SBRC algorithms.

Before illustrating the basic assumptions of the SBRC approach and the modeling in detail, some accuracy studies are performed in the following. Such an analysis is necessary for the verification of accuracy of the numerical solution. Also, this helps to examine the area of validity of the SBRC algorithms.

## 3.2 Accuracy study

In this thesis, the emphasis is placed on the analysis of signatures of the spatio-temporal evolution of fluid-induced microseismicity. In order to interpret the numerically simulated process of pore-pressure perturbation due to a fluid injection and the triggering of microseismicity, one has to verify the accuracy of the numerical method used here. Despite the insignificance of the absolute value of pore pressure for the purpose of this thesis, such an analysis is of importance for further developments of the method. In this chapter therefore a comparison of an analytical solution with the numerical solution of the modeling is shown. The analytical solution found is valid for the pressure perturbation due to a point source in a infinite 2D and 3D medium. The solution describes the pore pressure distribution after a certain time of the fluid injection at constant rate. A study is performed in order to find parameters for the finite-element grid size and source size. With this it is possible to guarantee minimal deviances between analytically calculated and modeled pore pressures.

In the following, analytical solutions for the heat distribution in a 2D and 3D, homogeneous isotropic medium as derived by Carslaw and Jaeger [1973] (chapter 10.2) are used. Pressure perturbation as well as heat transfer are described by the same diffusional kind of parabolic equation as described above. They similarly describe the heat and pressure distribution in a given medium. Here, only the main equations and results are shown. For a detailed derivation of the equations in 3D refer to Rentsch [2003].

### 3.2.1 Solution of the diffusion equation in 2D

The equation of diffusion for a homogeneous case in 2D reads

$$\frac{\partial p}{\partial t} = D\left(\frac{\partial^2 p}{\partial x^2} + \frac{\partial^2 p}{\partial y^2}\right), \tag{3.1}$$

where $D$ is the scalar hydraulic diffusivity of the medium, $p$ the pore pressure, $x,y$ the spatial coordinates and $t$ the time.

Let us assume a homogeneous, isotropic, infinite medium. Pressure is released at constant rate $\Phi(t) = q$ starting at $t = 0$ at a point $(x',y')$. Then, the solution at the time $t$ in a point $r$ becomes (compare Carslaw and Jaeger [1973], 10.4.II, page 261, eq. 5)

$$p(r,D,t) = -\frac{q}{4\pi D}\mathrm{Ei}\left(-\frac{r^2}{4Dt}\right), \tag{3.2}$$

where

$$-\mathrm{Ei}(-x) = \int_x^\infty \frac{e^{-u}}{u}du. \tag{3.3}$$

For the accuracy study presented here, results obtained by routines of the Numerical Recipes (Press et al. [2002]) are used. For a detailed description of the algorithm refer to chapter 6.3 of the afore mentioned book.

## Results

For the accuracy study, steps 1 and 2 are realized as presented in section 3.1. For this purpose, a hydraulically homogeneous and isotropic model is defined. Diffusivity is distributed homogeneously in the medium (defined as a scalar value). This value is used for the calculation of the analytic solution in equation (3.2). After obtaining the numerical solution of the diffusion equation, the results are analysed temporally and spatially. For the temporal analysis of pressure evolution, the FEM solution is extracted at specific points in the medium for all time steps. These points are characterized by their scalar distances $r$ relative to the injection source point. $r$ is used also in equation (3.2) where $t$ varies according to the numerically defined time steps. For the spatial analysis, the pressure amplitudes are extracted for specific times for all distances from the source to the model boundaries.

The result of the modeling of pressure perturbation for the 2D model is shown in figure 3.2(a). For distances $r$ =1, 2, 5, 10, 20 and 40m, the normalized time-dependent pressure is shown together with the analytically calculated one. For each distance, the mean error between numerical and analytical solution is calculated and given in table 3.1. The solution at $r > 10$m only differs by $< 5\%$ from the analytical one. In figure 3.2(b), results for the spatial comparison is shown. Here, after times $t$ =10, 20, 30, 40, 50 and 100 seconds, the distance-dependent pressure amplitude is plotted together with the analytical prediction. Figure 3.2 clearly indicates the accuracy between numerical and analytical solution. Moreover, table 3.1 quantitatively shows the small deviations of the two solutions. The deviations at $t$ =10s for distances larger than 35m give the numerical error.

### Source size

In the numerical modeling scheme, a finite area (circle or sphere of specific radius) of pressure perturbation is used. At the boundaries of this area, the initial pressure perturbation is defined. The analytical solution (equation 3.2) is valid for a point source. The consistency of analytical and numerical solution is better the smaller the source area is modeled. On the other hand, modeling time drastically increases with decreasing source size because of the mesh density at the origin. In order to find an optimal compromise between modeling time and accuracy, different source diameters are studied. The analytical and numerical solution are analysed and compared as described in the previous paragraph. For each model (different source diameters), the mean error of the two solutions for different distances in the medium are calculated. The results are shown in table 3.1. The error for all models and distances is found to be smaller than 10%. The qualitative observation that the error is larger for smaller distances is confirmed. Although, the quantitative difference is small.

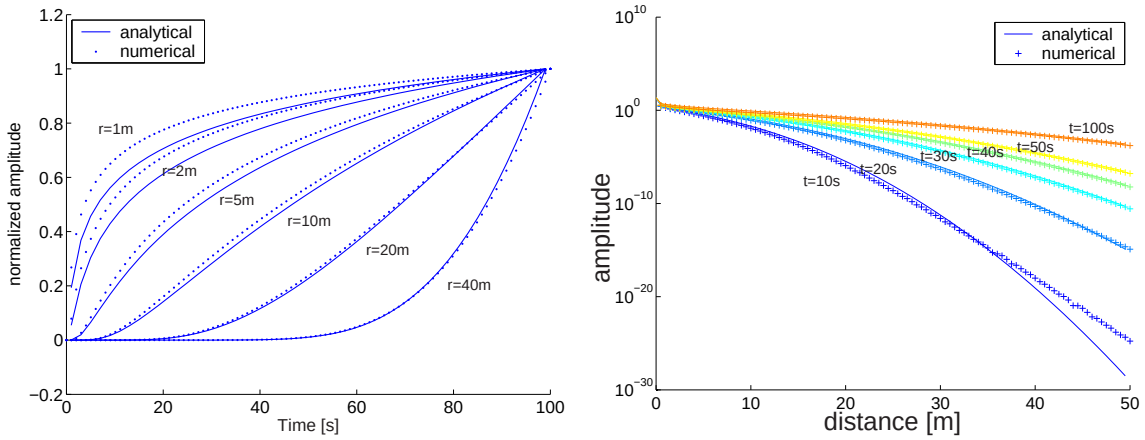


(a) (b)

Figure 3.2: Deviation of numerical and analytical solution obtained for a 2D homogeneous model with scalar hydraulic diffusivity of $D = 1\text{m}^2/\text{s}$. For the finite element scheme, a circular shaped pressure perturbation source of size $r_{src} = 0.001\text{m}$ and amplitude $A = 10$ was used. The mean errors are given in table 3.1. Left: normalized amplitude of time-dependent pore pressure perturbation for different distances from the source. Right: distance-dependent pore pressure for different solution times $t$.

The optimal compromise between modeling time and accuracy is found for a model with source of size $r_{src} = 10^{-4}$m. This source size is used for all 2D models in the following.

| mean error [%] | $r = 1$m | $r = 2$m | $r = 5$m | $r = 10$m | $r = 20$m | $r = 40$m |
|---|---|---|---|---|---|---|
| $r_{src} = 10^{-2}$m | 8.34 | 7.37 | 5.46 | 3.49 | 1.5 | 0.52 |
| $r_{src} = 10^{-3}$m | 5.29 | 4.65 | 3.4 | 2.1 | 0.8 | 0.52 |
| $r_{src} = 10^{-4}$m | 3.85 | 3.37 | 2.44 | 1.47 | 0.58 | 0.54 |
| $r_{src} = 10^{-5}$m | 3.01 | 2.63 | 1.88 | 1.12 | 0.45 | 0.63 |

Table 3.1: Mean deviation between numerical and analytical solution of pore pressure perturbation for models with varying source sizes. The errors are given in percent for different distances from the source location.

### 3.2.2 Solution of the diffusion equation in 3D

The equation of diffusion for a homogeneous case in 3D reads

$$\frac{\partial^2 p}{\partial x^2} + \frac{\partial^2 p}{\partial y^2} + \frac{\partial^2 p}{\partial z^2} = \frac{1}{D}\frac{\partial p}{\partial t} \tag{3.4}$$

where $D$ is the scalar hydraulic diffusivity of the medium, $p$ the pore pressure, $x, y, z$ are the spatial coordinates and $t$ the time.

It is assumed that the fluid injection source (in a borehole in real experiments) can be approximated by point source of constant pore pressure perturbation. The solution of equation (3.4) for the case of a infinite homogeneous isotropic 3D medium with a point source at $(x',y',z')$ is (Carslaw and Jaeger [1973], chapter 10.2., page 257)

$$p = \frac{\Phi(t)}{8(\pi Dt)^{\frac{3}{2}}} \exp\left(\frac{-[(x-x')^2+(y-y')^2+(z-z')^2]}{4Dt}\right). \tag{3.5}$$

If pressure is released with the rate $\Phi(t')$ per unit time from $t'=0$ to $t'=t$ at the point $(x',y',z')$, the pore pressure perturbation at $(x,y,z)$ at time $t$ is given by integrating equation (3.5),

$$p = \frac{1}{8(\pi D)^{\frac{3}{2}}} \int_0^t \Phi(t') \exp\left(\frac{-r^2}{4D(t-t')}\right) \frac{dt'}{(t-t')^{\frac{3}{2}}}, \tag{3.6}$$

where $r^2 = (x-x')^2+(y-y')^2+(z-z')^2$ (compare Carslaw and Jaeger [1973], 10.4.I, page 261).

This distribution of pore pressure perturbation is assumed to be due to a point source of the continuous strength $\Phi(t')$ from $t'=0$ onwards. If $\Phi(t')$ is constant there is no time dependence and $\Phi$ can be written equal to $q$. Using substitutions (see Rentsch [2003]), for the solution of the pore pressure perturbation $p$ the final result is obtained

$$p(r,D,t) = \frac{q}{4\pi Dr} erfc\left(\frac{r}{\sqrt{4Dt}}\right), \tag{3.7}$$

where the complementary Gaussian error function is defined as

$$erfc(x) := 1 - erf(x)$$

with

$$erf(x) = \frac{2}{\sqrt{\pi}} \int_0^x exp(-u^2)du, \qquad \lim_{x\to\infty} erf(x) = 1.$$

For infinite times equation (3.7) reduces to $p(r,D) = \frac{q}{4\pi Dr}$.

## Results

For the accuracy study in 3D, steps 1 and 2 are similarly realized as presented in section 3.1. A hydraulically homogeneous and isotropic model is defined. Equation (3.7) is used to calculate the analytical solution of pressure perturbation. After obtaining the numerical

solution of the diffusion equation, the results are analyzed in the same manner as explained for the 2D accuracy study. The result for the 3D model is shown in figure 3.3. On the left, for distances $r$ =10, 20, 30, 40, and 50m, the normalized time-dependent pressure behavior is shown together with the analytically predicted one. For each distance, the deviation between numerical and analytical solution is given in table 3.2. The largest deviation was found to be smaller than 5%. The distance-dependent pressure perturbation at specific times is shown in figure 3.3b and also indicates the match of analytical and numerical solution. The optimal compromise between modeling time and accuracy is found for a model with source of size $r_{src}$ =$10^{-2}$m. This source size is used for all 3D models in the following.

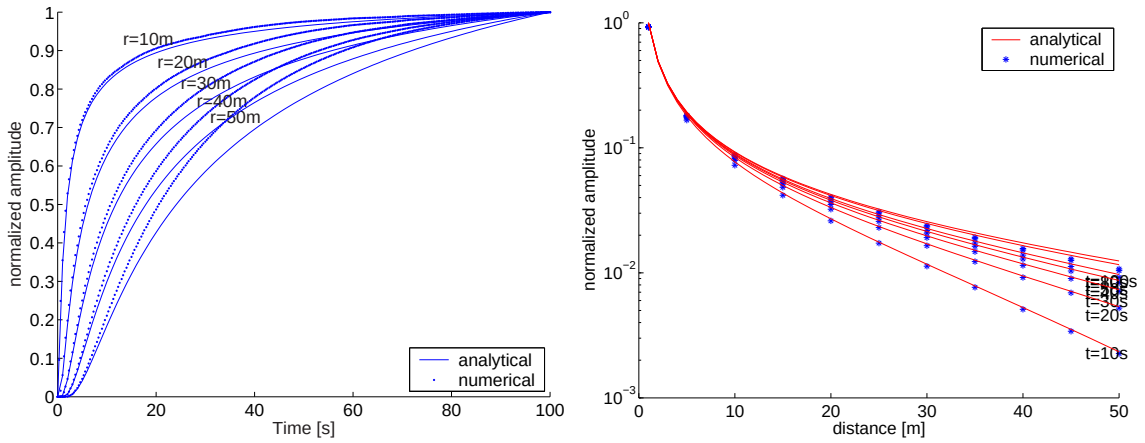


(a) (b)

Figure 3.3: Deviation of numerical and analytical solution obtained for a 3D homogeneous model with scalar hydraulic diffusivity of $D = 50\text{m}^2/\text{s}$. For the finite element scheme, a circular shaped pressure perturbation source of size $r_{src} = 0.1$m and amplitude $A = 10$ was used. The mean errors are given in table 3.2. Left: normalized amplitude of time-dependent pore pressure perturbation for different distances from the source. Right: distance-dependent pore pressure for different solution times $t$.

| mean error [%] | $r = 10$m | $r = 20$m | $r = 30$m | $r = 40$m | $r = 50$m |
|---|---|---|---|---|---|
| $r_{src}$= $10^{-2}$m | 0.74 | 1.68 | 2.59 | 3.67 | 4.94 |

Table 3.2: Mean deviation between numerical and analytical solution of pore pressure perturbation for a representative 3D model. The errors are given in percent for different distances from the source location.

## 3.3 Verification of eikonal approach

To verify the assertion that it is possible to describe the diffusion process and the kinematics of the evolution of the triggering front in a heterogeneous medium by the use of the eikonal solution (2.28) as described in chapter 2.2.1, numerical tests are performed. As described above, the parabolic differential equation of diffusion (2.1) in 2D is solved with the help

of the Finite Element Method. The time-dependent pressure variation through a medium where the diffusivity $D$ varies smoothly in $x$ direction with a Gaussian profile is calculated. It changes from a value of $D = 0.5\,m^2/s$ to a minimal value of $D = 0.1\,m^2/s$ at the center (compare figure 3.4b). The half-width of this heterogeneity is approximately 200 m. The dimension of the computational mesh is 4000 m x 4000 m, and the source point is located at its center. As input signal a time-harmonic sinusoidal signal with a period of 400 h and 800 h is used, respectively, multiplied with a boxcar function for the whole simulation time of 2400 h. The time increment in the simulations was $\Delta t \approx 3$ h while the elementary cell was of the order of 5 m x 5 m.

The pressure variation is observed in a one dimensional section along the x-axis through the center of the model, where the source is located. In each point of observation the arrival time of the fourth resp. sixth zero-crossing of our quasi-periodic pressure signal is estimated. This was necessary to reduce the effects of the high-frequency components due to the finite character of the source signal. This time is compared with the corresponding theoretical eikonal solution

$$t = \int_0^R \frac{dr}{v(r)}. \tag{3.8}$$

Using the arrival time also the velocity $v$ of the phase front at a given distance from the source point is calculated. Then the velocity is converted into the diffusivity and the result is compared with the exact diffusivity of the model. The diffusivity is calculated from the measured velocity of the phase front by

$$D(x) = \frac{v(x)^2}{4\pi f}, \tag{3.9}$$

where $f$ is the dominant frequency of the source function (see eq. 2.4 and the comment below).

Reasonable agreement between both numerical experiments is found. In figure 3.4a the traveltime is shown for the eikonal solution (equation 3.8) and the numerical results. Figure 3.4b shows the reconstructed diffusivity $D$ at a given distance $x$ in the medium. The good agreement between eikonal-predicted and numerically calculated travel times of the phase front in figure 3.4a is obvious. The small differences between the eikonal solution and numerical results at times $t < 50$ h can be explained with the relatively rough method used to pick the phase front, i.e. the zero-crossing.

The reconstructed diffusivity at a given distance in the medium also agrees well with the exact value (see. figure 3.4b). The differences at distances $x > 800m$ in figure 3.4b are caused mainly by influences of the prescribed boundary conditions, namely fixing the pressure to zero there (Dirichlet type). Thus the influences become larger at greater times and disturb the velocity of the triggering front measured during the numerical experiments. Differences between eikonal and numerical results are smaller for higher frequencies. This is obviously due to the fact, that the eikonal equation is a high frequency approximation, and therefore provides better results for smaller periods of the perturbation. In particular, the increasing

difference between theoretical curve and the models in figure 3.4b is due to the fact that the region of inhomogeneity, i.e. increasing diffusivity, is smaller than the wavelengths used. The small differences observed between estimated and exact diffusivities indicate that the formal validity conditions of the SBRC approach (equations 2.38-2.39) are too restrictive and the reconstruction algorithms are valid for a broader regime of frequencies.

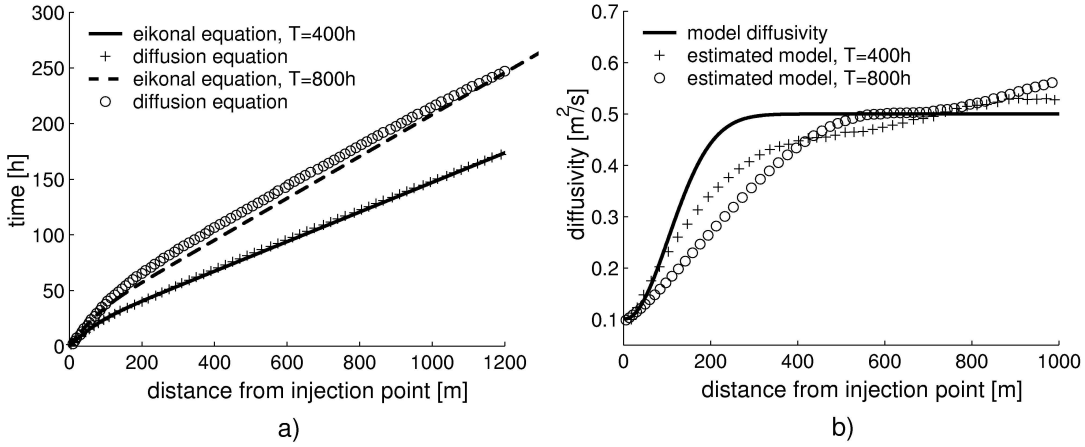


Figure 3.4: Comparison of eikonal equation and numerical diffusion models. (a) Traveltime of the phase front of the sinusodial signal versus distance from the source point. (b) Reconstructed hydraulic diffusivities from the traveltimes shown in (a) according to equation (3.9) for two different frequencies. The solid line corresponds to the hydraulic diffusivity distribution in the model (Gaussian shaped).

## 3.4 2D modeling and event triggering

### 3.4.1 Homogeneous isotropic case

Let us now continue to illustrate the modeling procedure and the simulation of the triggering of microseismic events due to a diffusive pore pressure perturbation process. This will be the subject of all further modeling considerations. Following the steps 1-5 explained in section 3.1, the approach starts at step no. 1 by defining a hydraulic model in the FEM scheme. The modeling dimension is 200 m $\times$ 200 m (200 m $\times$ 200 m $\times$ 200 m in three dimensions). A circular pressure perturbation source is centered in the model having a radius of $r$ =0.001 m ($r$ =0.1 m in 3D). The amplitude of pressure perturbation is defined as a boundary condition of the source circle/sphere in the FEM scheme. Therefore, the boundary of the source is assigned a specific value of perturbation. Generally, the shape as well as amplitude of the source signal can be arbitrary. In the following considerations, only the physical signature of event triggering is analyzed. Hence, an absolute dimension of the source amplitude is of no importance. In the first step, following the simplest assumption of the SBRC that the injection signal is a step function of constant amplitude, the value of initial pressure perturbation is chosen scalar and constant for all simulation times.

In the second step, the outer borders of the model are assigned a boundary condition of Dirichlet type, i.e., fixing the pressure solution to zero there. Because this procedure influences the pressure values near the borders, for further analyses only a subvolume of 100 m $\times$ 100 m (100 m $\times$ 100 m $\times$ 100 m in three dimensions) is extracted and studied. This ensures that artificial effects due to the boundary conditions are excluded. Next, the modeling area is assigned a diffusion coefficient as a subdomain condition. If we consider the model dimension in meters and modeling time in seconds, the corresponding dimension of the diffusion coefficient will be [$m^2$/s]. The value as well as distribution of the diffusion coefficient also can be arbitrary in general. In the next step, adequate solver types and iteration parameters are chosen. The output times of the solution are set to equally spaced time steps from zero to 100 (dimension is seconds here).

For the last step, the model is subdivided into small triangles (tetrahedra in 3D) which form the FEM mesh. The mesh size is chosen in order to find a optimal compromise of calculation time and accuracy. The set-up of the 2D hydraulic FEM model is shown in figure 3.5 (left). By running the numerical solver, the time-dependent solution of pressure within the model is obtained. In figure 3.5 (right) the solution is shown in the area of interest after the modeling time of 100 seconds. The color corresponds to the amplitude of pressure perturbation from zero to five. The source amplitude in this case was $A$=10. Additionally, isolines of constant pressure from 0.1 to 5 are shown here. The isolines form concentric circles which is expected because of the homogeneous and isotropic diffusivity model.

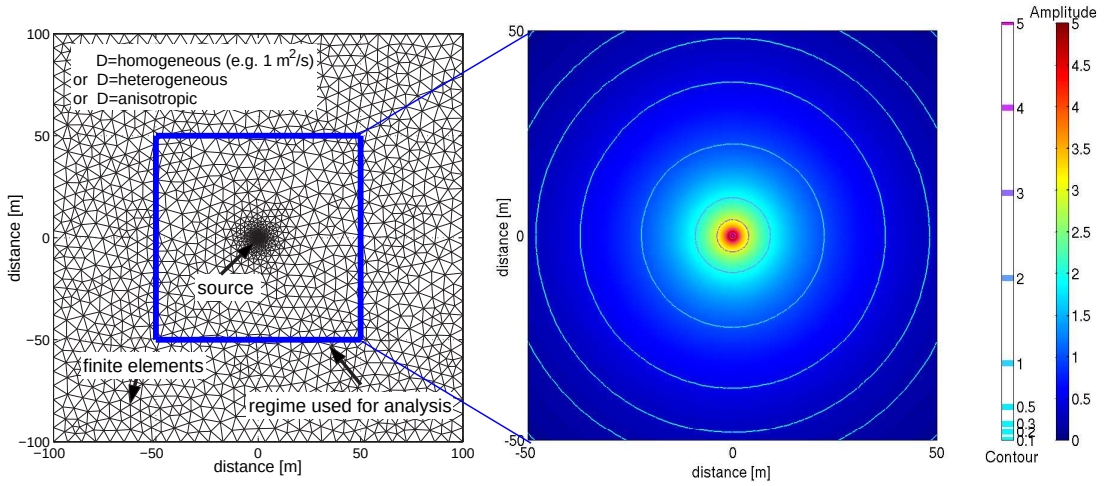


Figure 3.5: Numerical modeling in 2D. Left: Set-up of the hydraulic model with pressure perturbation source in the center. The medium is divided into triangular finite elements and the parabolic equation of diffusion is solved. The blue rectangle gives the area of investigation during further analysis steps. Right: Pressure perturbation after 100 seconds using a source amplitude of $A = 10$. The circles correspond to isolines of constant amplitudes.

After obtaining the solution of the diffusion equation for all time steps, the pressure values are interpolated on a rectangular grid. Despite the additional time consuming process, this step is necessary, because the SBRC approach assumes statistically even distributed zones of criticality in the medium. The grid size in 3D is optimized to fit a volume of

4.7 Gigabytes (DVD) with binary data in single precision format for all time steps. Total computing time for modeling the pressure perturbation and the interpolation for a 3D model is approximately 24 hours on a stand-alone, single-processor 2GHz PC.

Criticality $C$ is calculated which represents the model stability. $C$ corresponds to the stress which must be exceeded by pore pressure to trigger a seismic event. A simple example for statistically distributed criticality is shown in figure 3.6 (left). In this case, $C$ is distributed equally (a) or normally (c) between zero and a maximum criticality value. Color corresponds to the criticality of the medium. Blue colors denote small values, i.e. critical zones in the medium, whereas red colors denote high values, i.e. stable zones in the medium, respectively. The distribution function of the criticality criterion is shown on the right side of figure 3.6. Here, the number of cells containing a specific value of criticality are displayed in a bar diagram.

In the next step, the FEM solution of pressure perturbation, which was interpolated on the same grid, is compared with the criticality value. Therefore, within each cell $i$ and for each time step $t_j$, pressure $P_{i,t_j}$ is compared with failure $C_{i,t_j}$. An event is defined in such a cell, where $P_{i,t_j} > C_{i,t_j}$, i.e. the pressure exceeds the state of stress of the medium which leeds to failure and the triggering of a (seismic) event. Following this procedure, synthetic clouds of events are obtained.

Figure 3.7 shows the result of the modeling. The synthetic cloud of events generated during 100s of numerically simulated fluid injection using the criticality distributions shown in figure 3.6a consists of 604 events. Using the criticality distribution shown in figure 3.6b, 1706 events are triggered. Colors correspond to event occurrence times. Evidently, the same spatio-temporal growth observed for real data can be observed here regarding numerically created data (compare figure 2.4).

In figure 3.8 the estimation of the scalar hydraulic diffusivity using equation (2.6) is shown for the data set shown in figure 3.7. It is obvious, that the spatio-temporal distribution of the events agrees well with the behavior predicted by this equation. The triggering front corresponding to the value of diffusivity used in the homogeneous model ($D = 1\,\mathrm{m}^2/\mathrm{s}$) is indicated by the solid line according to equation (2.6). 95.19% (a) and 95.53% (b) of all events triggered are located below this line.

It is interesting to note that in spite of the simplicity of this modeling approach the synthetic cloud of events show the most important characteristic features of microseismic clouds obtained in reality: it has a characteristic parabolic envelope (compare this with figure 2.4 in chapter 2, where real data have been plotted).

### 3.4.2 Trigger criterion statistics

The SBRC approach assumes a medium which is in some kind of critical state of stress. The number of critical points are assumed to be distributed equally in space. Following this idea, the criticality $C$ was calculated in the modeling approach shown in the previous

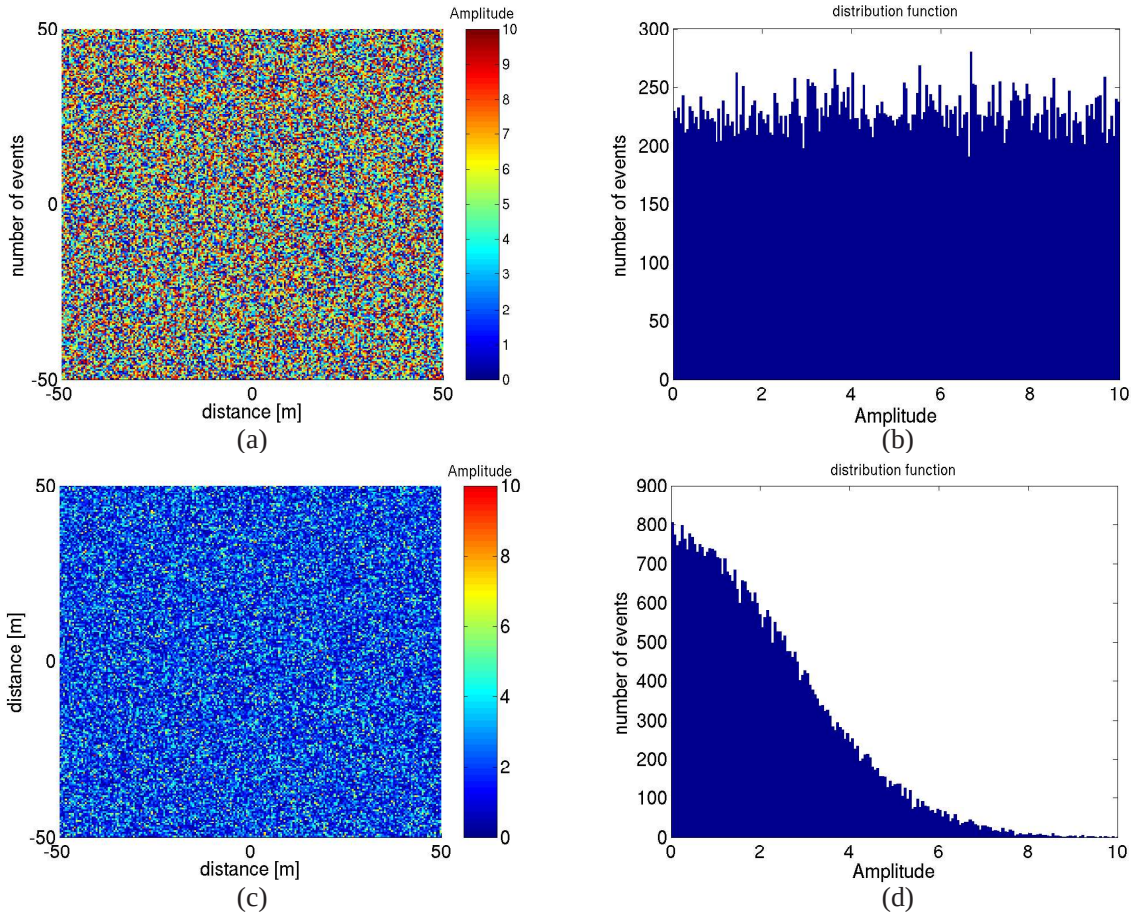


Figure 3.6: (a) and (c) Two examples for criticality ($C$) distributions in 2D. Random numbers are distributed in rectangular cells within a definite range of amplitudes. For the two criticality fields, different distribution types were used which are shown in (b) and (d). For (a) an even distribution was used, for (c) a normal distribution, respectively.

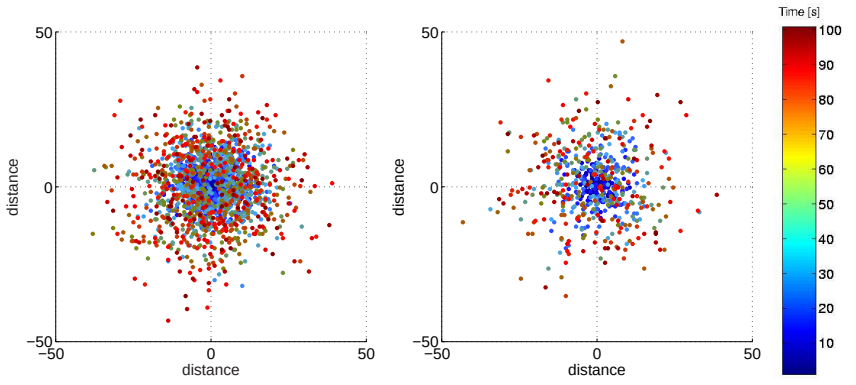


Figure 3.7: Clouds of events after triggering in a homogeneous, isotropic 2D medium. (a) Cloud triggered using the criticality shown in figure 3.6a. (b) Cloud triggered using the criticality shown in figure 3.6c. Colors correspond to the event occurrence times.

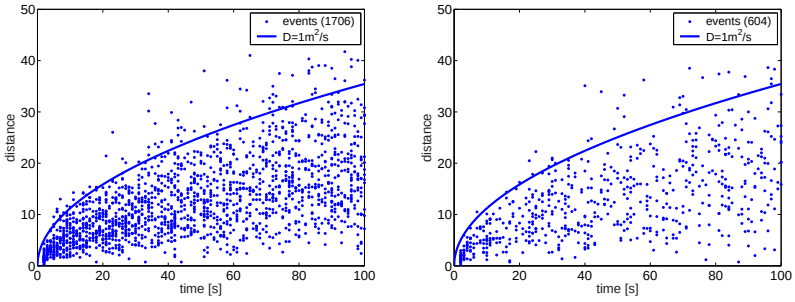


(a) (b)

Figure 3.8: Estimation of effective scalar hydraulic diffusivity using the hypocenter and time coordinates of the event clouds shown in figure 3.7. The blue envelope is calculated according to equation (2.6) using the hydraulic diffusivity of the model ($D = 1$ m$^2$/s). (a) Estimation using the cloud of events shown in figure 3.7a, (b) estimation using the cloud of events shown in figure 3.7b.

section. In order to study the influence of different distribution types, an equal distribution (figure 3.6a) as well as a normal distribution function was successfully studied (figure 3.6c). The normal or even distribution of critical points in real rocks is just a rough approximation. Real rocks mostly contain heterogeneities which can be expressed as a heterogeneous distribution of the criticality field. In order to model the triggering of seismic events in such media, the influence of different criticality statistics on the triggering of microseismicity is analyzed here.

In geophysics, real rock-like media and the distribution of heterogeneities can be described using mathematical methods like spatial autocorrelation functions. Here, such media are simulated by calculating spatially correlated random fields of the criticality. We consider random media that are characterized by the second-order statistics concerning the distribution of critical points. The realizations of the random medium have a certain mean value and a spatial correlation function defined by the correlation length $a$ and the variance $\sigma$.

A random medium realization can be generated by taking the inverse Fourier transform of the spectrum of normally distributed fluctuations (with Gaussian probability density function with zero mean and unit variance) multiplied with the sqare root of the fluctuation spectrum (the random numbers of criticality in our case)

$$C_{corr} = \mathcal{F}^{-1}\left[\mathcal{F}(C) \quad \cdot \quad \Phi^{2D/3D}(ACF)\right], \tag{3.10}$$

where $\mathcal{F}$ denotes the Fourier transform, $C$ the original field of uncorrelated random criticality numbers and $\Phi^{2D/3D}$ the power spectral density function (PSDF, Fourier transform of the autocorrelation function). $\Phi^{2D/3D}$ represents the spectrum of fluctuations in the medium. We use two types of autocorrelation functions: exponential and Gaussian, respectively. Below, the correlation functions of Gaussian and exponential type and their 2-D and 3-D Fourier transforms are shown (Müller [2001]).

| **Type** | **ACF(*r*)** | $\phi^{2D}(k)$ | $\phi^{3D}(k)$ |
|---|---|---|---|
| Exponential | $\sigma^2 e^{-\vec{r}/a}$ | $\frac{\sigma^2 a^2}{2\pi(1+k^2a^2)^3/2}$ | $\frac{\sigma^2 a^3}{\pi^2(1+k^2a^2)^2}$ |
| Gaussian | $\sigma^2 e^{-\vec{r}^2/a^2}$ | $\frac{\sigma^2 a^2}{4\pi} e^{-k^2a^2/4}$ | $\frac{\sigma^2 a^3}{8\pi^{3/2}} e^{-k^2a^2/4}$ |

Table 3.3: Exponential and Gaussian autocorrelation functions and their Fourier transforms $\Phi$ (pseudo spectral density functions) in 2D and 3D.

---

$a$ is the correlation length of the heterogeneities, $\sigma^2$ the variance of criticality, $r$ the coordinate vector and $k$ the frequency vector.

By using different probability-density types for the criticality as well as correlating it spatially (e.g., with Gaussian or exponential autocorrelation functions) the influence of different types of criticality statistics on the triggering process can be studied. For example, a structure of critical zones can be included in the models. In figure 3.9 an exponentially correlated distribution of the criticality is shown. The synthetic event clouds obtained after triggering are shown in figure 3.10. In figure 3.11, a Gaussian-correlated distribution of the criticality is shown. The synthetic event clouds obtained after modeling/triggering are shown in figure 3.12.

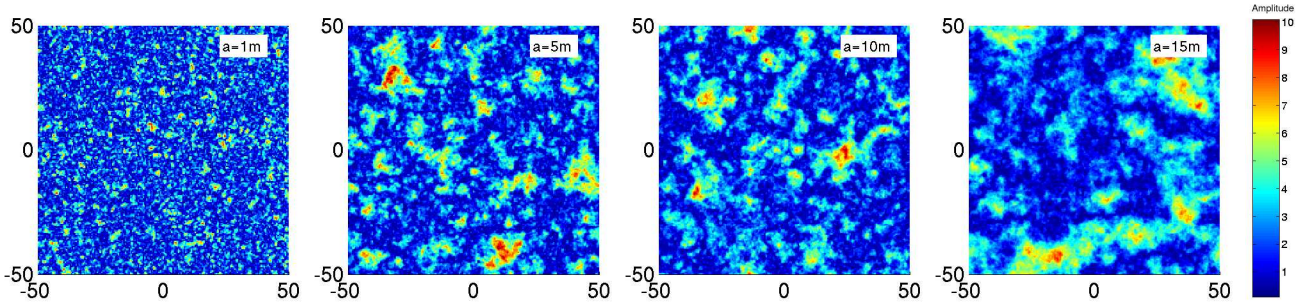


Figure 3.9: Distribution of criticality $C$ using a spatial autocorrelation function of exponential type according to equation (3.10). From left to right: increasing correlation length $a$ (1m, 5m, 10m and 15m). The colorbar gives the criticality value.

All clouds of events shown in figure 3.10 and 3.12 are analyzed in terms of the SBRC method using equation (2.6). The results are shown in figure 3.13. Percentage of events below the envelope function for all models are given in table 3.4. Here, another physical feature often observed in reality is obvious: a parabolic zone of low event density (see all figures in 3.13. A strip of low event density for distances smaller than $5-10m$) looking like a "back triggering front" can be also usually observed in reality (compare again with figure 2.4 in chapter 2). The main result of this modeling is the fact, that the spatial correlation of the criticality (i.e. the second statistical moment) does not seem to influence the estimation of effective scalar hydraulic diffusivity strongly. The first statistical moment, i.e., the distribution type of the criticality itself (normally or equally), however seems to

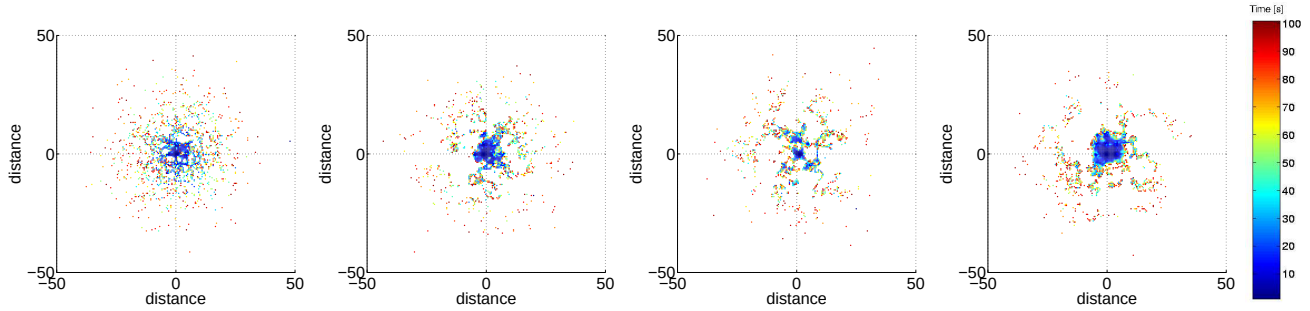


Figure 3.10: Event clouds triggered in a hydraulically homogeneous, isotropic medium with $D = 1$ m$^2$/s using the criticality distributions shown in figure 3.9.

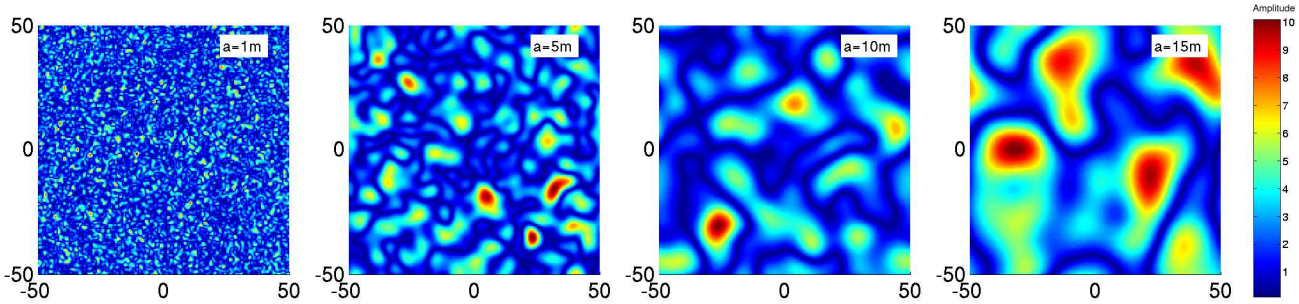


Figure 3.11: Distribution of the criticality $C$ using a spatial autocorrelation function of Gaussian type according to equation (3.10). From left to right: increasing correlation length $a$ (1m, 5m, 10m and 15m). The colorbar gives the criticality values.

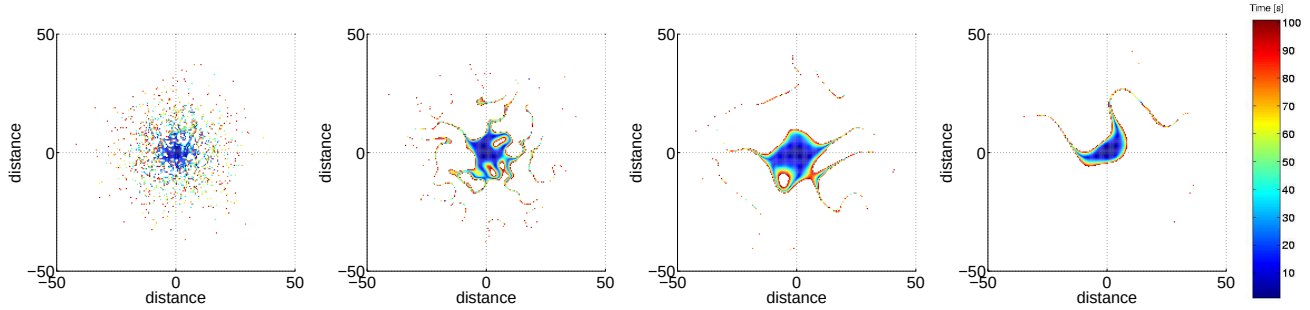


Figure 3.12: Event clouds triggered in a hydraulically homogeneous, isotropic medium with $D = 1$ m$^2$/s using the criticality distributions shown in figure 3.11.

| model | 1 | 2 | 3 | 4 | 5 | 6 | 7 | 8 |
|---|---|---|---|---|---|---|---|---|
| events below envelope [%] | 95.2 | 94.3 | 93.5 | 95.8 | 94.6 | 96.2 | 96.4 | 90.9 |

Table 3.4: Percentages of events below the parabolic envelope according to equation (2.6) for models containing spatially correlated criticality.

have a stronger effect on the results. The variation of the first statistical moment results in the change of number/density of events and therefore effects the estimation of the fitting envelope.

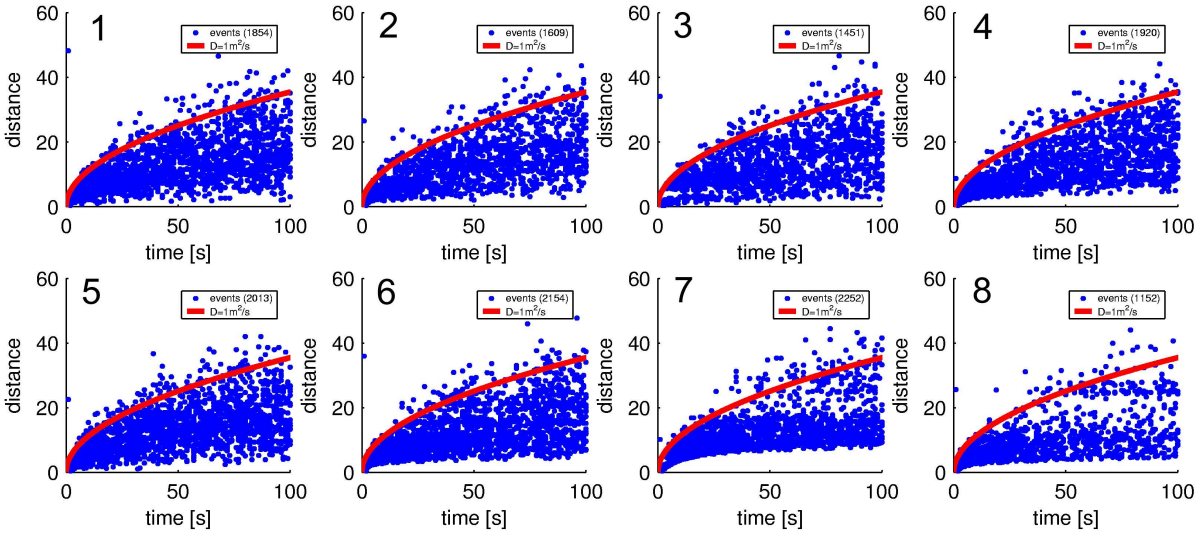


Figure 3.13: Estimation of effective scalar hydraulic diffusivity using the hypocenter and time coordinates of the event clouds shown in figures 3.10 (1-4) and 3.12 (5-8). The envelope is calculated according to equation (2.6) using the hydraulic diffusivity of the model ($D = 1$ m$^2$/s).

Another important observation obtained using this modeling approach is that there are at least two physically different quantities whose heterogeneous distributions in space strongly influence the appearance of microseismicity clouds. The first one is the triggering critical pressure which was studied so far. The second one is the hydraulic diffusivity. Models with heterogeneously distributed diffusivity in 2D will be considered in the following section.

### 3.4.3 Heterogeneous case

The numerical modeling procedure demonstrated above does not only allow to study the triggering phenomenon within hydraulically homogeneous and isotropic media. It also provides the possibility to include any desired type of hydraulic model. Media with heterogeneously distributed hydraulic diffusivity can be treated as well as anisotropic ones (see section 3.5.3). In figure 3.14a, an example for a simple heterogeneous model is shown. Two values of scalar diffusivity are used. The cross-shape structure is characterized by

an increased value of diffusivity ($D_1 = 50\text{m}^2/\text{s}$), whereas its value in the surrounding regions is chosen 10 times smaller ($D_2 = 5\text{m}^2/\text{s}$). As an input signal a step-function pressure perturbation with constant amplitude in the center of the model is used.

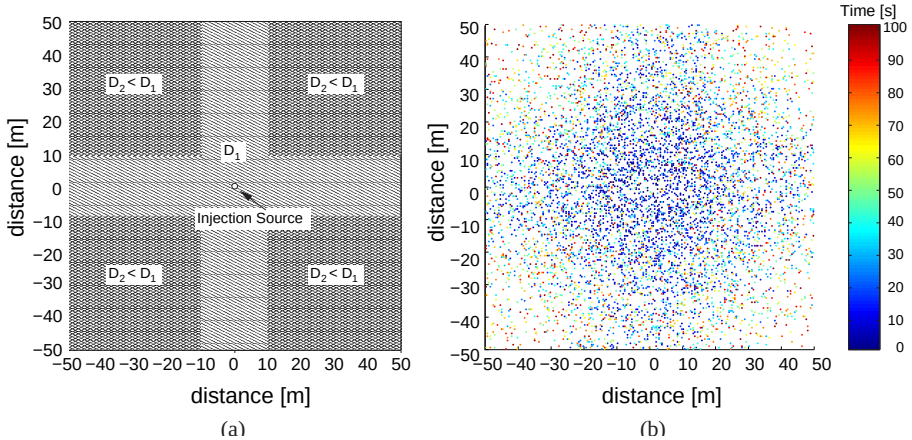


Figure 3.14: Left: Hydraulically heterogeneous model consisting of a cross structure shaped area of high and borders of low hydraulic diffusivities. Right: Event cloud triggered after 100 seconds of modeling. Colors correspond to event occurrence times.

The result of the modeling is shown in figure 3.14b. A total of 20337 events were triggered. The estimation of scalar hydraulic diffusivity from this data set is shown in figure 3.15a. The coordinates of the events in the space-time domain are shown as blue dots, the curves represent the two values of hydraulic diffusivity used in the model according to equation (2.6). It is obvious, that even for this model the spatio-temporal structure of the events fulfill the behavior predicted by equation (2.6). 99.91% of all events are located below the envelope with $D = 50\text{m}^2/\text{s}$. Thus, the SBRC-algorithm based on equation (2.6) for estimation of maximum scalar hydraulic diffusivity works quite well even for heterogeneous media.

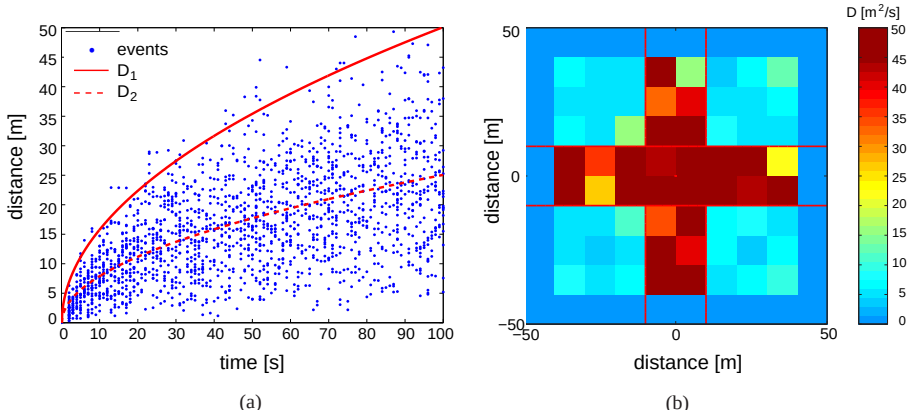


Figure 3.15: Reconstruction of effective hydraulic diffusivity and diffusivity distributions in 2D for the hydraulic heterogeneous medium shown in figure 3.14 according to equations (2.6) and (2.34). Left: The two envelope functions were computed using the two different hydraulic diffusivities of the heterogeneous model.

Let us now test the SBRC eikonal-equation based inversion algorithm for the reconstruction

of diffusivity distributions in space. The distribution of hydraulic diffusivity in the model shown in figure 3.14a is reconstructed by applying the SBRC-algorithm on the basis of equation (2.28). The model is subdivided into 10 $\times$ 10 cells each containing 475 events in average. Triggering time is then defined in each cell and equation (2.28) is used directly for estimating $D$ (see Shapiro et al., 2002 and Shapiro, 2000). The result of the inversion procedure is shown in figure 3.15b. The overall structure (cross-shape) of the medium is reconstructed. The inversion approach was also tested on other synthetic models and usually a well reconstructed distribution of hydraulic diffusivity was received. A second example of hydraulically heterogeneous structure is shown in the following.

In the second example of heterogeneous modeling and reconstruction, the model shown in figure 3.16a was used. Here, a circular shaped heterogeneity of increased diffusivity was embedded into a homogeneous background. The hydraulic heterogeneity was shifted from the source location (at $x,y$=0) by $x$=-25m. Therefore, no 'hydraulic' connection between pressure source and the heterogeneity exists. The radius of the circle was set to $r$=20m. In figure 3.16b the solution of the diffusion equation after modeling time $t$=100s is shown. Additionally, isolines of constant amplitudes are shown in order to clarify the increased diffusivity regime within the circular area.

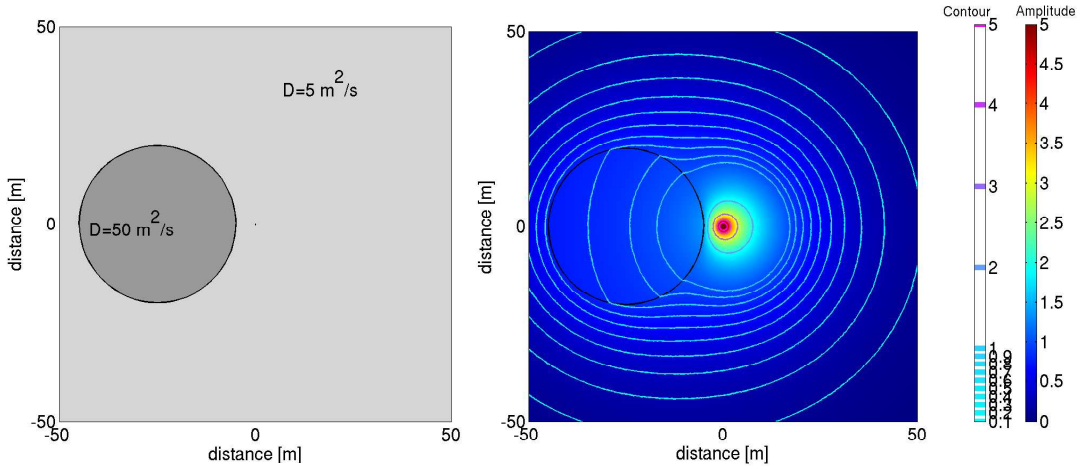


(a) (b)

Figure 3.16: Second example for a hydraulic heterogeneous model. (a) Schematical sketch of the numerical model. Within a homogeneous background of $D_1 = 5\text{m}^2/\text{s}$, a circle of increased hydraulic diffusivity ($D_1 = 50\text{m}^2/\text{s}$) is embedded. The heterogeneity has a radius of $r$=20m centered at $x$=-25m, $y$=0m. (b) Solution of the pressure perturbation after $t$=100s. The color denotes the pressure amplitude. Isosurfaces are shown as solid lines.

For modeling, the criticality shown in figure 3.17 (left) was used. It was distributed normally between 0 and 2. On the right side of figure 3.17 the cloud of events triggered after the modeling procedure is shown. The hypocenters and times of the events are used for the reconstruction of hydraulic diffusivity. The distribution of hydraulic diffusivity for the model shown in figure 3.16a is reconstruced by applying the SBRC-algorithm on the basis of equation (2.28) for the data set shown in figure 3.17 (right). The model is subdivided

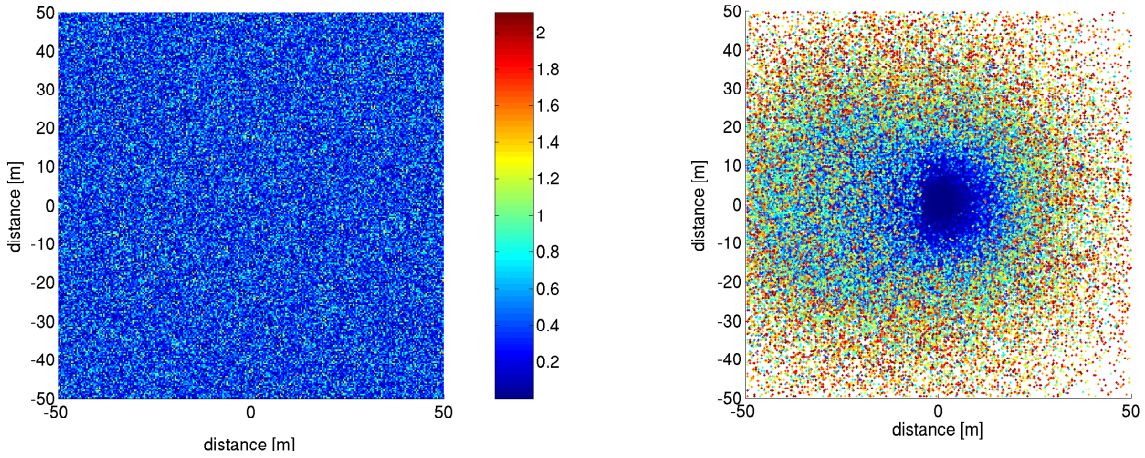


Figure 3.17: Left: Distribution of the criticality. It was distributed between 0 and 2 with a normal distribution function. Right: Cloud of events after numerical triggering. The color denotes the event occurence times. A total amount of 41908 events were triggered.

from 10×10 up to 20×20 cells, iteratively. Triggering time is then defined in each cell and equation (2.28) is used directly for estimating $D$. The result of the inversion procedure is shown in figure 3.18. In subfigure (a), 100% of all events induced were used for the triggering time computation. In figure 3.18b, the earliest 5% of the events were removed, which corresponds to a 95% fitting criterion as it will be explained later in chapter 3.5.2.

The results clearly shows that the structure (circular-shaped region of increased hydraulic diffusivity) in the medium is reconstructed quite well for all refinement steps. This once more supports the applicability of the eikonal-equation based inversion (equation 2.28) of microseismic data.

## 3.5 3D modeling and event triggering

### 3.5.1 Homogeneous isotropic case

The modeling of the triggering phenomenon of induced microseismicity in 3D is performed analogous to the approach presented in chapter 3.4. Now, the three-dimensional parabolic equation of diffusion (3.2.2) is solved by the FEM solver for a model of 100m side length. After interpolating the solution onto a rectangular grid, the criticality (trigger criterion) is similarly computed and distributed within space. An uncorrelated normal or even distribution of the trigger criterion can be simulated as well as correlating it spatially following the approach of section 3.4.2. Examples of uncorrelated and correlated criticalities are shown in figure 3.19. An equal distribution of random numbers within a given range of amplitude is shown (3.19a) beneath a exponentially (3.19b) or Gaussian correlated criterion (3.19c).

The result of the triggering process is shown in figure 3.20. A total amount of 7506, 12738

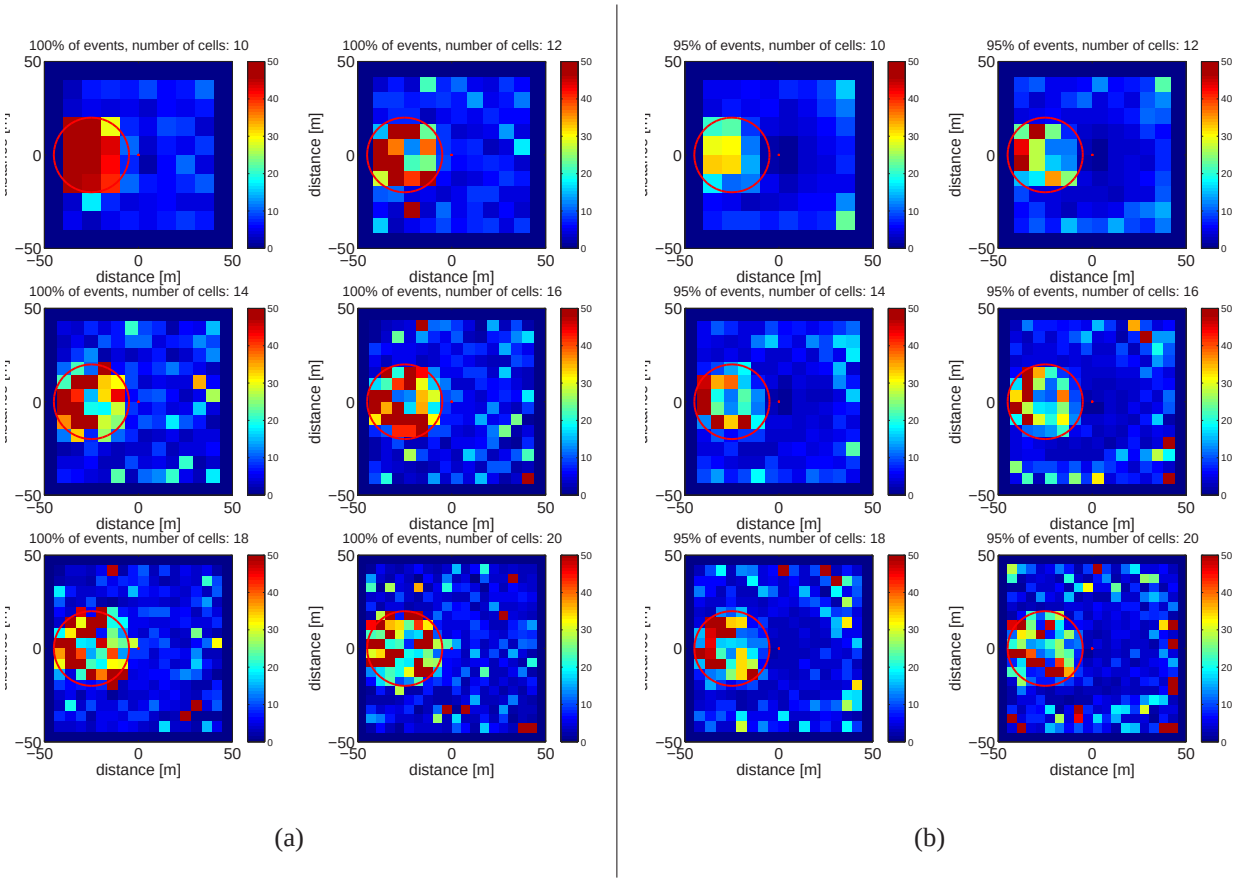


Figure 3.18: Reconstruction of hydraulic diffusivity in 2D for different cell sizes. (a) 100% of the events were used, (b) the first 5% of the earliest events were removed for the analysis. The red circle denotes the heterogeneity used in the hydraulic model.

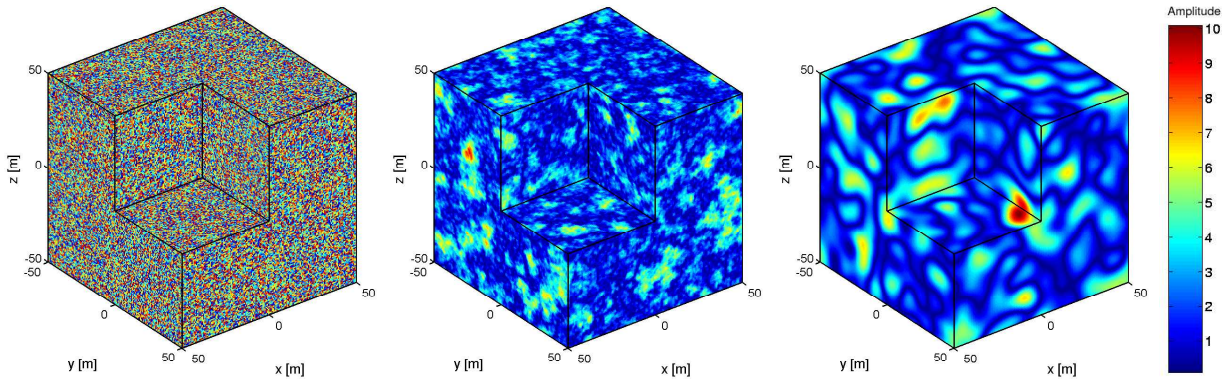


(a) (b) (c)

Figure 3.19: Distribution of the criticality in 3D using no correlation function (a), an exponential ACF with $a$=10m (b) and a Gaussian ACF with $a$=10m (c). (b) and (c) are computed according to to equation (3.10). The color corresponds to the criticality value.

and 6561 events were triggered during the simulated injection, respectively. The estimation of scalar hydraulic diffusivity ($r$-$t$-plot) from the data sets is shown in figure 3.21. The coordinates of the events in the space-time domain are shown as blue dots, the curve represents the value of hydraulic diffusivity used in the model according to equation (2.6). It is obvious, that even for these models the spatio-temporal structure of the events fulfill the behavior predicted by equation (2.6). 95.1% (3.21a), 95.2% (3.21b) and 94.7% (3.21c) of all events are located below the envelope-function with $D = 5\text{m}^2/\text{s}$, respectively.

For this model, a maximum pressure perturbation $P$ was reached at the borders of the model after a simulation time of $t$ =100 s large enough to trigger events. The maximum scalar distance of these outer events relative to the source point is $r_{max} = \sqrt{50\text{m}^2 + 50\text{m}^2 + 50\text{m}^2} = 86.6\text{m}$. The theoretical distance of the triggering front for this model according to equation (2.6) for $t$ =100 s is $r_{front} = 79.3\text{m}$. Nevertheless, the amplitudes of maximum pressure at the borders are small compared to the criticality values (distributed between 0 and 10 in this case). The probability, that events are triggered near the borders of the model therefore is low. A higher probability would have been achieved by decreasing the maximum criticality value resulting in a larger number of triggered events at the borders. The low probability for triggering and therefore small event number in this case explains the apparent saturation of event density at approximately 70m in figure 3.20. Thus, the estimation of effective scalar hydraulic diffusivity shows, that the SBRC-algorithm based on equation (2.6) for estimation of maximum scalar hydraulic diffusivity works quite well for 3D media, too.

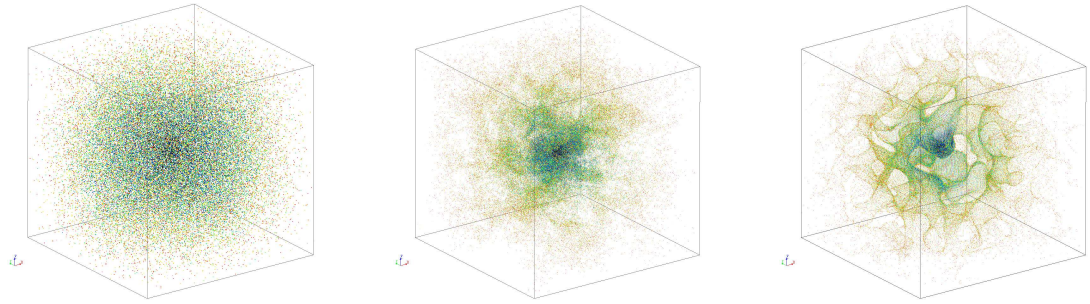

(a) (b) (c)

Figure 3.20: Event clouds triggered in a 3D hydraulically homogeneous, isotropic medium with $D = 5$ m$^2$/s using the criticality distributions shown in figure 3.19. Color corresponds to the event occurence times.

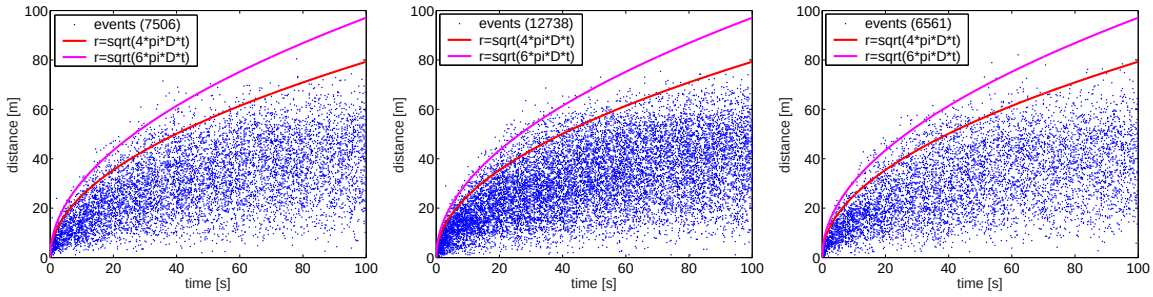


Figure 3.21: Estimation of effective scalar hydraulic diffusivity using the hypocenter and time coordinates of the 3D event clouds shown in figure 3.20. The envelope is calculated according to equation (2.6) using the hydraulic diffusivity of the model ($D$ =5 m$^2$/s).

### 3.5.2 Envelope fitting criterion

For real data, the estimation of the parabolic envelope in a distance-versus-time (*r*-*t*) diagram is a fundamental step. Despite the importance only of dimensions of magnitudes of hydraulic diffusivity, a criterion for fitting must be defined. So far, a percentage criterion was used, e.g., 92% to 95% of all events must be located below the envelope function calculated according to equation (2.6). The question arises if a more quantitative criterion can be defined. The numerical modeling approach proposed in this thesis may help finding such a criterion as well as modifications of the SBRC algorithms in order to yield more precise estimates of diffusivity.

In the FEM modeling scheme, only the parabolic equation of diffusion is solved. Therefore, the only process simulated so far is the process of pore pressure perturbation. This is done in accordance to the main assumption of the SBRC approach, that a diffusional process of this kind is the dominant one for triggering microseismic events at least in most cases. Within the SBRC approach, equation (2.6) was derived describing the spatial position of the triggering-front as explained in chapter 2. This front corresponds to the time-dependent boundary between unperturbated and perturbated regimes in the medium. The equation describing the front's position was derived in a quasi-heuristical way. Moreover, it denotes a 'sharp' position for the triggering-front due to pore pressure perturbation. E.g., the factor $4\pi$ is just an approximation in the equation for the position of the triggering front. However, the process of pressure perturbation is of diffusional kind and therefore does not provide sharp boundaries. In fact, the position of the front triggering microseismic events can be $r = \sqrt{(4\pi \pm \varepsilon) Dt}$.

In order to derive a criterion for envelope fitting or modification of equation (2.6), the events induced using 3D modeling are statistically analysed: Following equation (2.6), each event of a given cloud (submodel) is assigned its theoretical diffusivity calculated by

$$D_{event} = \frac{r_{event}^2}{4\pi t_{event}} \tag{3.11}$$

Given that the true value $D$ of hydraulic diffusivity of the model is known, one can count the percentage of events that fulfill the criterion $D_{event} < D$. By varying the value of $D$, a statistical analysis shown in figure 3.22 is obtained. Here, for the model `m002` (see appendix, table of models), this percentage-curve is plotted versus the diffusivity for submodels 1-16, 17-30 and 100-150, respectively. The red dashed line corresponds to the input value of $D$ used in the model. For all models, regardless criticality variations or correlation, about 95% of the events are located below the theoretical envelope according to equation (2.6). About 100% of events underlie an envelope calculated with an increased hydraulic diffusivity of $D = 7\text{m}^2/\text{s}$. Therefore, by fitting the clouds of events with a 100%-criterion would overestimate the effective hydraulic diffusivity by 40% for this model.

Another statistical analysis is shown in figure 3.23. Here, for models `m011`, `m012`, `m013` and `m014` for each model the percentage of events that fulfill equation (3.11) is plotted. For the different models, criticality as well as first and second statistical moment is varying

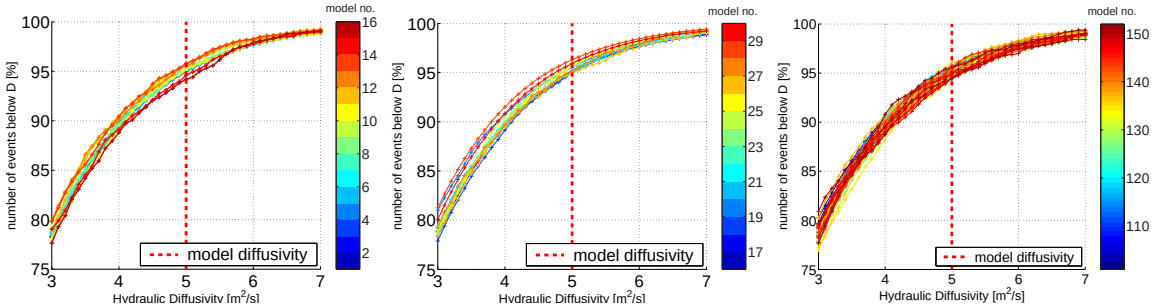


Figure 3.22: Model `m002`: Statistical analysis of the percentages of events below the parabolic envelope according to equation (2.6). Left: Models 1-16 without correlation of criticality. Middle and right: different models with varying criticality and Kaiser effect (see below, chapter 3.5.6).

according to table A.2. The horizontal red line corresponds to the input value of hydraulic diffusivity. The results clearly show the overestimation of $D$ by 30-40% when fitting all events below an envelope. This overestimation leads to the suggestion to modify the heuristic factor in equation (2.6) towards larger values. Assuming a 100%-criterion for fitting, this factor would change from $4\pi$ to approximately $6\pi$:

$$r_{old} = \sqrt{4\pi Dt} \quad \Rightarrow \quad r_{new} = \sqrt{6\pi Dt} \tag{3.12}$$

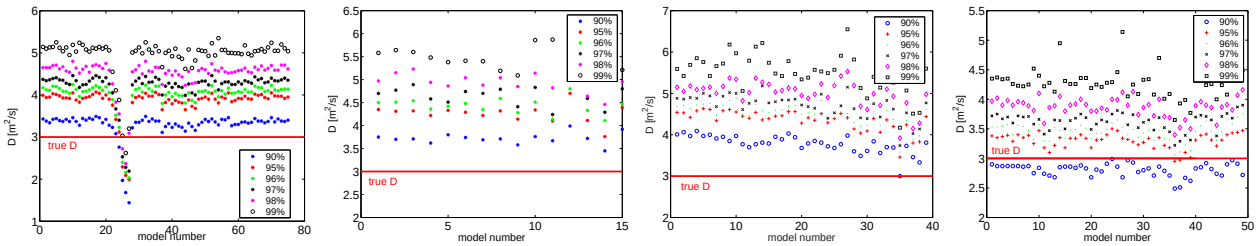


(a) (b) (c) (d)

Figure 3.23: Estimation of effective scalar hydraulic diffusivity according to equation (2.6) for models (a) `m011`, (b) `m012`, (c) `m013` and (d) `m014` and each submodel. Colors correspond to different percentage criteria for the number of events that satisfy equation (2.6). Note, that the group of outliers in figure (a) is an effect of the submodels 23-28 of `m011`, where the Kaiser effect has been modeled (see chapter 3.5.6). This effect resulted in a very small number of events triggered. The statistical analysis of the event clouds failed because of insufficient data.

Another important analysis is the dependence of event numbers triggered with medium criticality. Let us assume a given pore pressure perturbation in the medium. Then, the probability for events triggered is larger the smaller the critical pore pressure in the model is. In other words, the smaller the range of criticality values the higher is the number of triggered events. One assumption is, that the number of events in dependence of the medium criticality fulfill the following equation

$$N \propto \frac{1}{C_{max}}, \tag{3.13}$$

where $N$ corresponds to the number of events triggered and $C_{max}$ is the maximum criticality (Shapiro, pers. comm.). In figure 3.24 such an analysis is shown for model `m002`. The blue stars denote the total amount of triggered events for different submodels in dependence of the maximum medium criticality (compare appendix, table of models). The red solid line was calculated using equation (3.13) normalized on the maximum event number. The results clearly show the excellent correlation between medium criticality and number of events released. This confirmation of equation (3.13) leaves room for further potential developments of the SBRC approach analysing event rates (see chapter 6.2).

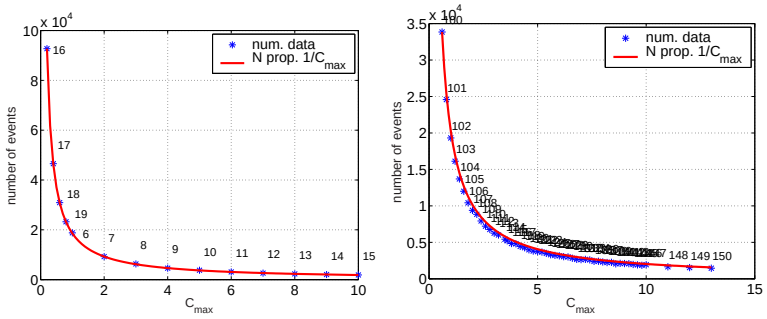


Figure 3.24: Numerically computed event numbers and analytically predicted event numbers versus criticality maximum for model `m002`. Numbers at the stars denote the 'submodel' number where statistical model parameters like distribution type and spatial correlation of criticality ($C_{max}$) changed (compare table A.2).

### 3.5.3 Anisotropic case

In reality, rocks are often characterized by anisotropy in respect of their seismic or hydraulic properties. In order to simulate the process of pore pressure diffusion in such a case, one has to extend the numerical modeling procedure presented above. Anisotropy is assumed to be of hydraulic nature, i.e., the medium is characterized by an anisotropic tensor of hydraulic diffusivity. Besides modeling hydraulically homogeneous or heterogeneous media, it is also possible to simulate hydraulic anisotropy with the scheme proposed in section 3.1 by the following approach: A simple way to model anisotropy is to define the principal components $D_{11}, D_{22}$, and $D_{33}$ of the diffusivity tensor $\mathbf{D}$. However, in this case the axis of the tensor are still parallel to the axis of the Cartesian coordinate system. In order to simulate an arbitrarily rotated tensor, all components of the symmetric tensor $\mathbf{D}$ have to be specified. Given the principal components of the tensor and the angles of rotation around the $x, y$ and $z$ direction ($\alpha, \beta$, and $\varphi$, respectively), the computation of the symmetric diffusivity tensor with no entries equal to 0

$$\mathbf{D_{ij}} = \begin{pmatrix} D_{11} & 0 & 0 \\ 0 & D_{22} & 0 \\ 0 & 0 & D_{33} \end{pmatrix} \quad \Longrightarrow \quad \mathbf{D_{ij}^{new}} = \begin{pmatrix} D_{11} & D_{12} & D_{13} \\ D_{21} & D_{22} & D_{23} \\ D_{31} & D_{32} & D_{33} \end{pmatrix} \tag{3.14}$$

is done by the following transformation (in matrix notation using summation over repeating indices):

$$\mathbf{D}_{\mathbf{ik}}^{\mathbf{new}} = \mathbf{A}_{\mathbf{ij}} \cdot \mathbf{A}_{\mathbf{kl}} \cdot \mathbf{D}_{\mathbf{jl}} \qquad (i,j,k = 1,2,3). \tag{3.15}$$

Here, **A** is the matrix consisting of the unit vectors in $x,y$, and $z$ direction of the new coordinate system. **A** is obtained by matrix multiplication of the unit vectors of the Cartesian coordinate system $\vec{e}_x = [1\ 0\ 0]$, $\vec{e}_y = [0\ 1\ 0]$, $\vec{e}_z = [0\ 0\ 1]$ and the rotation matrix **R** (Großmann [1993])

$$\mathbf{R} = \begin{pmatrix} \cos(\varphi)\cos(\beta) & \sin(\varphi)\cos(\alpha) - \sin(\beta)\cos(\varphi)\sin(\alpha) & -\sin(\varphi)\sin(\alpha) - \sin(\beta)\cos(\varphi)\cos(\alpha) \\ -\sin(\varphi)\cos(\beta) & \cos(\varphi)\cos(\alpha) + \sin(\varphi)\sin(\beta)\sin(\alpha) & -\cos(\varphi)\sin(\alpha) + \sin(\varphi)\sin(\beta)\cos(\alpha) \\ \sin(\beta) & \cos(\beta)\sin(\alpha) & \cos(\beta)\cos(\alpha) \end{pmatrix}.$$

Note, that the unit vectors of **A** must be orthogonal and `det=+1`. Parameters for different hydraulically anisotropic models are given in table A.1. The new hydraulic diffusivity tensor is implemented into the FEM modeling scheme as subdomain diffusion coefficient.

Results of the numerical modeling of anisotropic diffusion are shown in figure 3.25. Here, the pressure perturbation is shown in 3D from different directions after a modeling time of $t$ =100 s on three orthogonal slices parallel to the Cartesian $x,y$ and $z$ axis, respectively. The color corresponds to the pressure perturbation. Additionally, in figure 3.25(b-d) isosurfaces of pressures $P = 0.05$ and $P = 0.01$ are shown in order to point out the anisotropic diffusion.

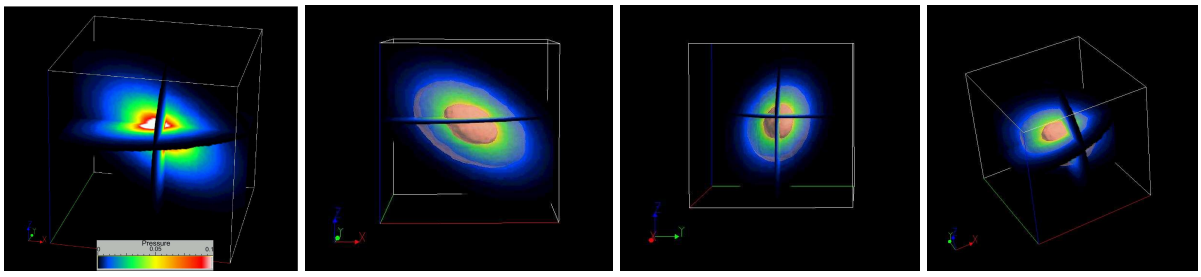

(a) (b) (c) (d)

Figure 3.25: Pore pressure perturbation after $t$ =100s for 3D diffusivity model `m007`. Here, hydraulic diffusivity was distributed anisotropically with the diagonal elements of the tensor $D_{xx} = 1\text{m}^2/\text{s}$, $D_{yy} = 2\text{m}^2/\text{s}$ and $D_{zz} = 5\text{m}^2/\text{s}$, respectively. Additionally, the tensor is rotated by 60°, 30° and 0° around the $x$-, $y$- and $z$-axis according to equation (3.15). In (b)-(d) two isosurfaces of pressure were added.

The cloud of events triggered after the anisotropic modeling together with the pressure perturbation is shown in figure 3.26(a-b). By applying equation (2.6) the result shown in figure 3.26c is obtained. Also here, the reconstruction of effective scalar hydraulic diffusivity is successfully performed. As already pointed out by Shapiro et al. [1999a], in the case of 3D anisotropy, equation (2.6) yields the estimation of the arithmetic average value of **D**. Therefore, for the calculation of the fitting envelope in figure 3.26c, a value of $D = \frac{trc(\mathbf{D})}{3}$ was used.

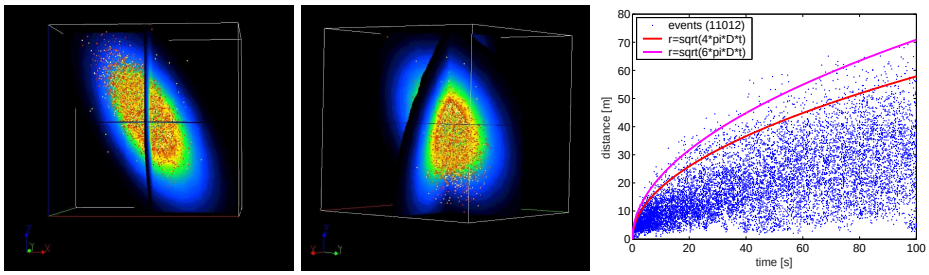


(a) (b) (c)

Figure 3.26: (a) and (b): Anisotropic pressure perturbation for model `m007` together with the cloud of events triggered after numerical modeling. (c) Estimation of effective scalar hydraulic diffusivity from $r-t$-plot. The envelopes were computed using the mean value of the diagonal tensor of hydraulic diffusivity $\bar{D} = \frac{D_{11}+D_{22}+D_{33}}{3}$. The red (lower) envelope was calculated using equation (2.6), the magenta (upper) envelope using a corrected factor there of $6\pi$, respectively.

By modeling anisotropic pressure perturbation, it is possible to verify the tensor reconstruction approach as proposed by Rindschwentner [2001] and Shapiro et al. [2003]. Therefore, here the approach proposed and explained in detail by Rindschwentner [2001] is applied. By transferring the coordinates of the events from the original into a scaled coordinate system (scaling with equation 2.9), the fitting of the cloud of events with an envelope ellipsoid in 3D can be performed. Then, the half axes of this envelope ellipsoid correspond to the square roots of the principal diffusivities. Also, the orientations of the principal axes are obtained.

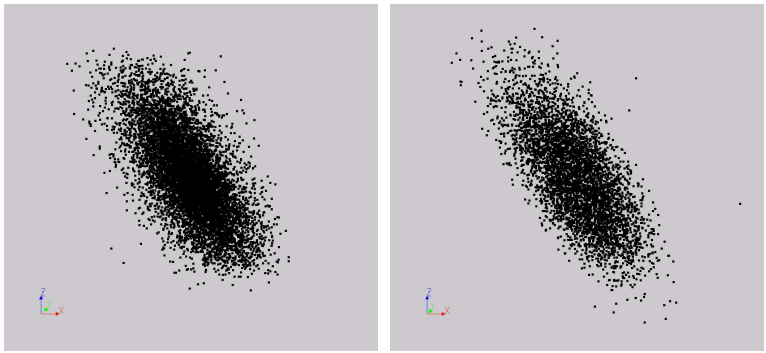

(a) (b)

Figure 3.27: Data for model `m007` in the a) unscaled and b) scaled coordinate system.

The result of this analysis is shown in figure 3.27. Here, a data set created after numerical triggering is shown in the unscaled (3.27a) and in the scaled (3.27b) coordinate system. The ellipsoidal envelope estimated by using equation (2.10) is shown in figure 3.28 from the south, east and top. The tensor of hydraulic diffusivity used for modeling and the reconstructed tensor components are given in the table below. According to equations

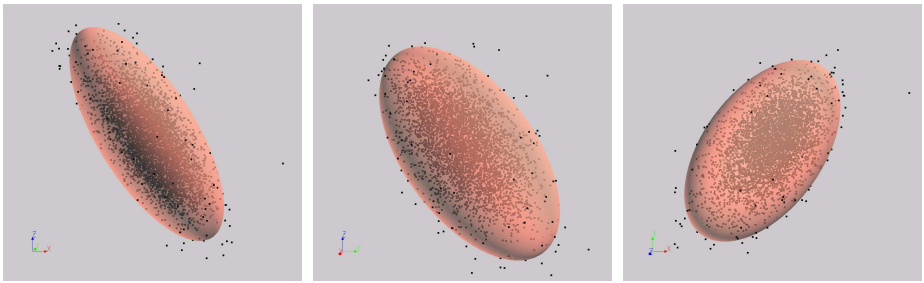

(a) (b) (c)

Figure 3.28: Reconstructed tensor of hydraulic diffusivity for the event cloud shown in figure 3.27 in the scaled coordinate system. a) View from the south, b) from the east and c) from the top. The original tensor components used for modeling were $D = \mathrm{diag}(1,2,10)$. The reconstructed hydraulic diffusivity tensor after 'unscaling' was $D = \mathrm{diag}(1.12, 2.10, 8.64)$.

(3.40-3.43c) of Rindschwentner [2001], the latitude and longitudes (strike and dip) of the principal tensor axes $\vec{x},\vec{y}$ and $\vec{z}$ are given in table 3.5 for the tensor orientation. The strike of the vector is counted up clockwise from north (old $y$-direction) and positively from the horizontal upwards and negatively downwards.

| | $D_{11}$ | $D_{22}$ | $D_{33}$ | $\mathrm{lat}_{\vec{x}}$ [$^o$] | $\mathrm{lat}_{\vec{y}}$ [$^o$] | $\mathrm{lat}_{\vec{z}}$ [$^o$] | $\mathrm{lon}_{\vec{x}}$ [$^o$] | $\mathrm{lon}_{\vec{y}}$ [$^o$] | $\mathrm{lon}_{\vec{z}}$ [$^o$] |
|---|---|---|---|---|---|---|---|---|---|
| model | 1 | 2 | 10 | 30 | 25.66 | 48.59 | 90 | 343.90 | 22.89 |
| reconstructed | 1.12 | 2.10 | 8.64 | 30.75 | 26.62 | 47.17 | 92.31 | 344.96 | 222.24 |
| error [%] | 12 | 5 | 13.6 | 2.5 | 3.7 | 2.9 | 2.6 | 0.3 | 0.6 |

Table 3.5: Modeled and reconstructed components of the diffusivity tensor and its orientation.

The latitude and longitude of the diffusivity axes given in the table 3.5 for the numerical modeling correspond to rotation angles $\alpha = 30^o, \beta = 30^o$, and $\varphi = 0^o$, respectively. The results support the practicability of the 3D tensor reconstruction algorithms proposed in the SBRC approach.

### 3.5.4 Source functions

The SBRC approach assumes triggering of microseismicity due to a step function like process of pore pressure perturbation. In most cases of real injection experiments, the source function can be approximated by such a step function. However, in some cases this assumption and such an approximation is not valid. Therefore, in order to extensively study the effects of different source type functions on the triggering, the modeling approach is adapted accordingly. In figure 3.29 four different types of source signals are shown and

used for modeling. In figure 3.29a, a 'normal' step function source of constant amplitude for all time steps (100 seconds) is shown. In figure 3.29b, the injection signal is switched off, i.e. exponentially damped to zero, after $t = 40$s (red) and after $t = 20$s (blue), respectively. Figure 3.29c shows the characteristics of a real hydraulic injection experiment performed in 1994 at the German Continental Deep Drilling site (KTB). For more details refer to chapter 4.

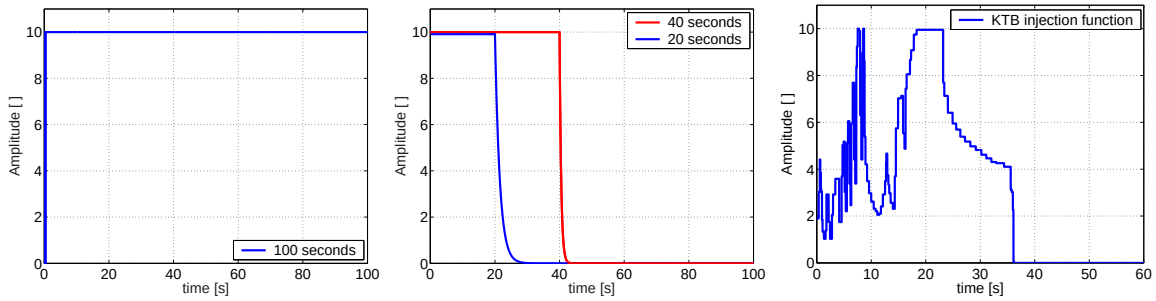


Figure 3.29: Different source functions used for modeling. a) Step function of constant amplitude for all time steps, b) constant pressure perturbation exponentially turned off at $t = 40$s and $t = 20$s, c) source function interpolated from a real hydraulic injection experiment (KTB 1994, see chapter 4).

For all different source signals modeling was successfully conducted. Despite the necessity of enhanced solver parameters and increased computation time, numerical triggering of events was performed. In figure 3.30, the event rates (number of events within a discrete time interval) for every modeled source function are shown. As assumed for the case of the constant step function, the event rate also remains constant as far as the model boundaries are not reached. In the case of the damped injection signals, also the event rates decrease after the pressure perturbation was stopped (figure 3.30b). It is an interesting result to observe, that despite the turning-off of the pressure perturbation triggering continues for all further time steps. Only the number of events decrease, in dependence on the cut-off shape and/or hydraulic diffusivity of the model. Also for the case of the simulated real injection signal (figure 3.30c), the event rate is strongly correlated with the injection signal. At times where the pressure perturbation reached a maximum, also a maximum in the number of events is obtained. This opens the idea for possible correlation studies of injection signal and event rate. This point will be discussed again later on and in further sections (e.g chapter 4). A detailed study of this aspect of the triggering phenomenon and the extension of the SBRC approach is not subject of this thesis. For more details refer to Parotidis and Shapiro [2004].

All data created with different types of injection signals are analysed in terms of the SBRC method and equation (2.6). The results are shown in figure 3.31. For all numerically created event clouds, the estimation of effective scalar hydraulic diffusivity is successfully performed. The envelopes shown were computed using the scalar, homogeneous value of hydraulic diffusivity of the model. Even in the case of the real injection signal (3.31c), the estimation of maximum scalar diffusivity is possible, despite of the very complex event rate and spatio-temporal distribution of the events.

An interesting result of this modeling step is the so-called 'back triggering front' which also

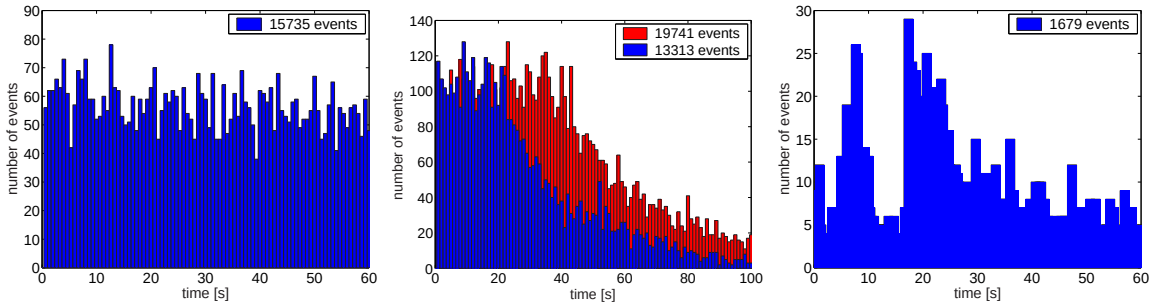


Figure 3.30: Event rates for the source functions shown in figure 3.29. In all cases a strong correlation of the source shape function and event rate can be observed.

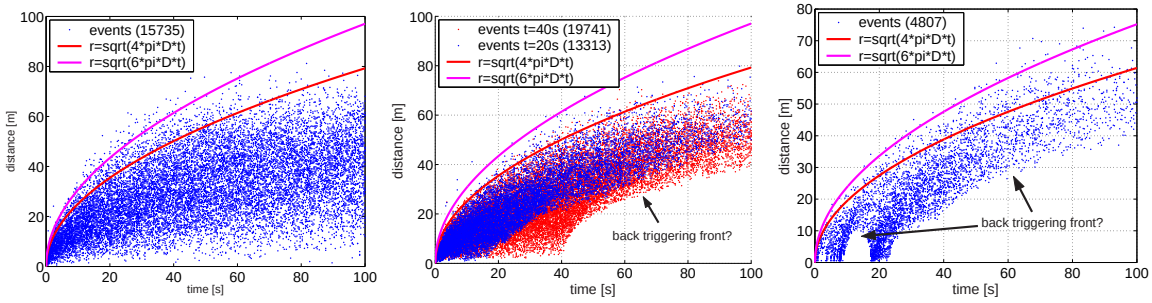


Figure 3.31: Estimation of effective scalar hydraulic diffusivities for models created by using the source functions shown in figure 3.29. The blue and red dots correspond to the events. The two solid envelopes were calculated using the scalar diffusivity of the hydraulic model with and without corrected heuristic factor (see equation 3.12).

can be observed in real data very often. This front is clearly observable in figures 3.31b and 3.31c. As already mentioned before, triggering of events still continues, when the source perturbation is switched off. However, triggering occurs at distances far away and stops near the pressure perturbation source just immediately after shutoff. Then, a front of low event density is formed. First analyses show that the shape of this 'back triggering front' also depends on the hydraulic diffusivity used in the model. The idea arises to further study the correlation of the back front and the injection signal. A possible extension of the SBRC method towards the analysis of event rates or back fronts is promising but not subject of this thesis. For more details refer to Parotidis et al. [2004].

### 3.5.5 Source geometry

In most cases real injection experiments can be approximated by a point source of constant pressure perturbation. This is the main assumption of the SBRC method as described in chapter 2. However, in some cases the fluid loss and therefore pressure perturbation can occur within a extended interval, e.g. open hole section or perforated borehole casing interval. In such a case, the SBRC approach has to be modified. An example for the analysis of data created during such a type of experiment was proposed by Audigane [2000]. Here, a modification of the SBRC algorithms for estimation of effective scalar hydraulic diffusivity substantiated by numerical experiments is proposed.

In figure 3.32 the geometry of the model used for this analysis is shown. The 3D model is designed in the same way as explained in chapter 3.5. Diffusivity is defined homogeneous and isotropic with $D = 1\text{m}^2/\text{s}$. Now, instead of a sphere approximating the point source of pressure perturbation, a cylinder of length 30m and radius 0.5m is centered in the model. As boundary condition, a constant value of pressure perturbation is defined in the FEM model.

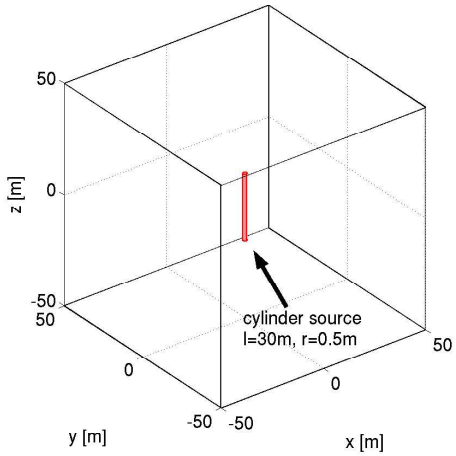


Figure 3.32: 3D model for an extended pressure perturbation source. In the center of the model, a cylinder of length 30m and radius 0.5m is located. A constant pressure perturbation is defined as boundary condition.

The FEM solution of the diffusion equation for this model is shown in figure 3.33 after

different modeling times. The amplitude of pressure is shown on the *yz*-plane at $x = 0$. The results clearly indicate the cylindrical region of pressure perturbation at small times. For times larger than approximately 40 seconds, the isosurfaces of pressure become nearly spherical again, at least large distances from the source line.

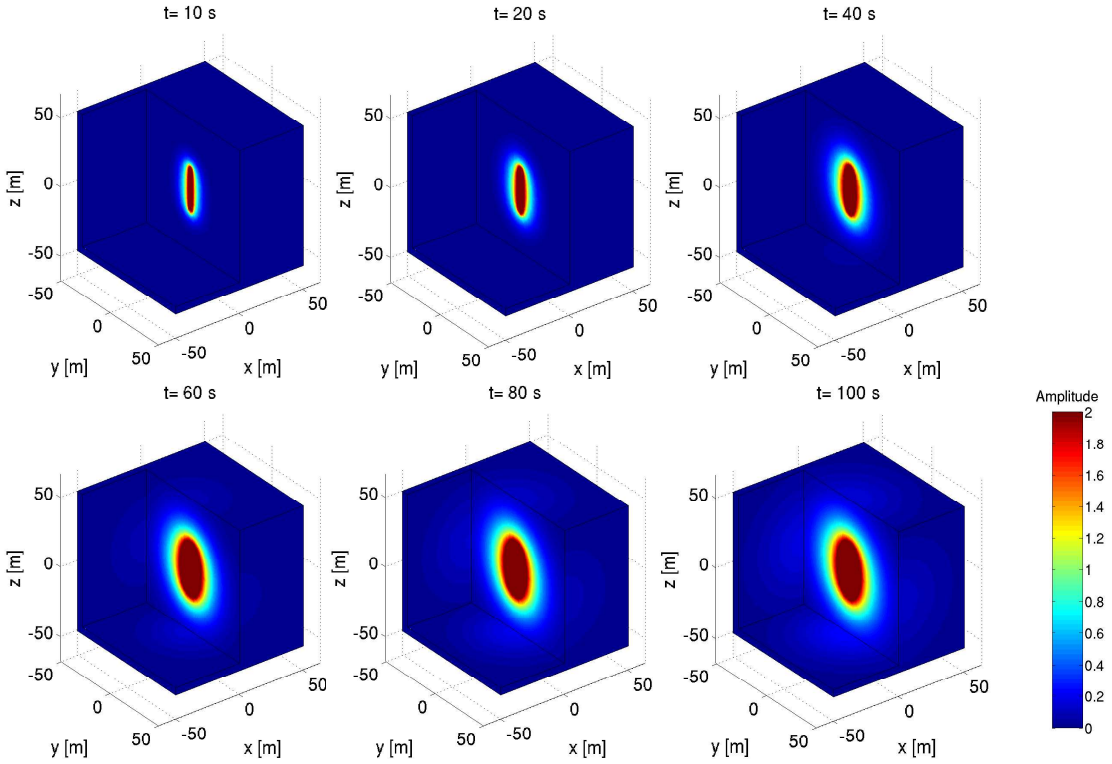


Figure 3.33: Solution of the diffusion equation for different time steps of modeling. As source, a cylindrical pressure perturbation of constant amplitude was used.

After numerical triggering, the cloud of events shown in figure 3.34 containing 41004 events is obtained. The hypocenters are shown at the same time steps as in figure 3.33. For small times, the cylindrical extension of the cloud is clearly observable. The result of the estimation of effective scalar hydraulic diffusivity using equation (2.6) is shown in the $r-t$ plot in figure 3.35 (left). At small times the extension of the cloud of events up to 30m can be observed. For all times, a large amount of events is located above the theoretical envelope. Therefore, hydraulic diffusivity will be overestimated by fitting the unmodified cloud in the $r-t$ plot.

Now, the following modification is proposed in order to correct the cloud of events for the line/cylinder source: In this case, the length of the injection line was $l$ =30m. The line source was centered at $x,y,z = 0$ in the model with its main axis parallel to the $z$-axis. Now, all events induced after modeling time having a $z$-coordinate $|z| > 15$m will remain unchanged. The scalar distance relative to the injection interval is the minimal distance to

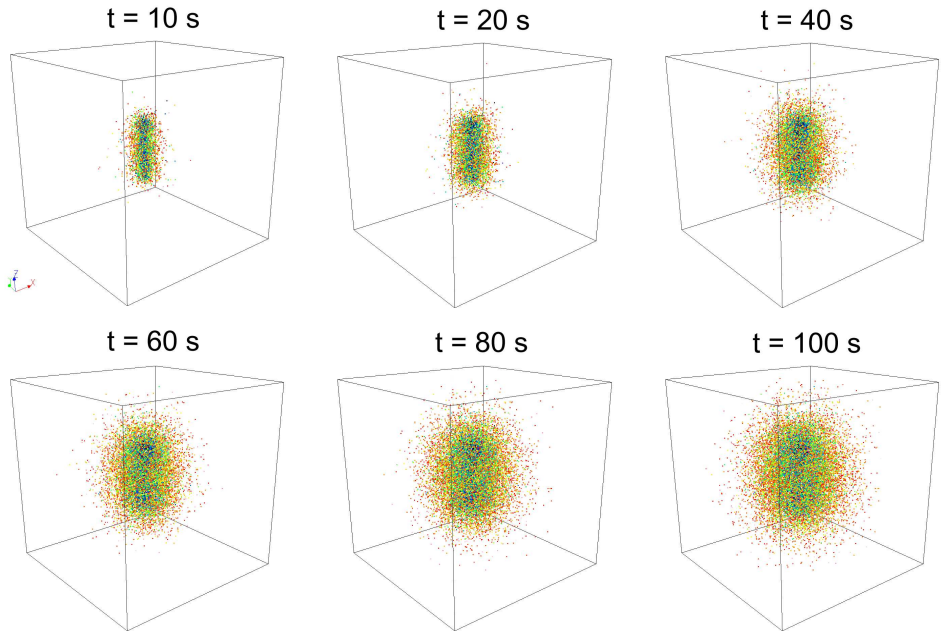


Figure 3.34: Cloud of events induced for the cylindrical pressure perturbation source model. The locations of the events are shown for the same times as in figure 3.33.

the top or bottom of the line source

$$\begin{aligned} r_{z>15\text{m}} &= \sqrt{x^2+y^2+z^2-z_{top}} \\ r_{z<-15\text{m}} &= \sqrt{x^2+y^2+z^2-z_{bottom}} \end{aligned}$$

with $z_{top}$ =15 and $z_{bottom}$ =-15. The scalar distance of events having coordinates of -15m $< z <$ +15m are calculated according to

$$r_{-15<z<15\text{m}} = \sqrt{x^2+y^2},$$

which means the calculation of the minimum distance of these events relative to the line source.

The result of this simple modification of the event coordinates is shown in figure 3.35 (right). Here, events with $z >$ 15m are shown in red, those with $z <$ -15m in blue and events in between in green, respectively. The result clearly shows that the scalar estimation and fitting with the 'correct' envelope now is straightforward. For the unmodified coordinates, only 66.1% of all events are located below the envelope calculated according to equation (2.6) in the $r-t$ plot (figure 3.35 left). For the modified hypocenters, 91.0% are located below the theoretical curve (right). Moreover, 97.5% of the events are located below the modified envelope as proposed in chapter 3.5.2 (equation 3.12) with and 81.2% without a correction, respectively.

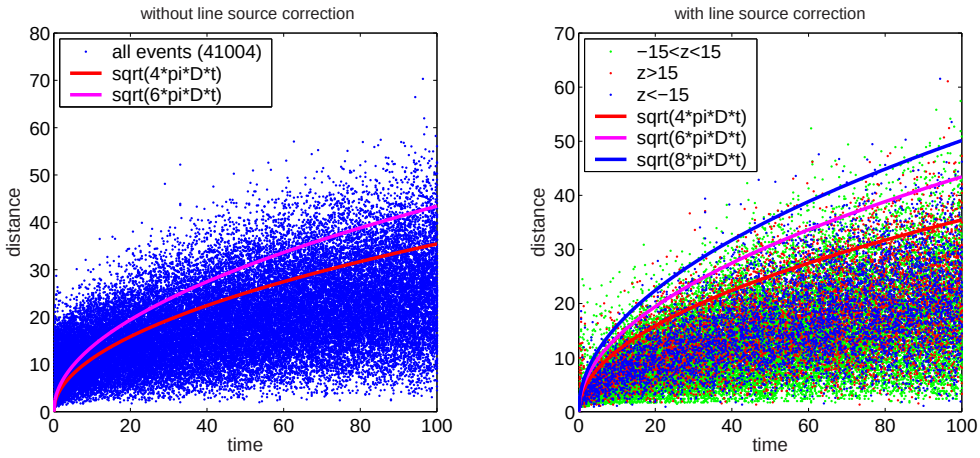


Figure 3.35: Estimation of effective scalar hydraulic diffusivity from the cloud shown in figure 3.34. At the left: original form of the algorithms without a correction for the cylindrical source. Right: modified algorithm with source correction (equation 3.12).

### 3.5.6 Kaiser effect

So far, numerical modeling of the SBRC approach supports the concept of triggering of microseismicity due to a diffusive process of pore pressure perturbation. Reconstruction of hydraulic diffusivity is successful for all models analyzed. However, the modeling approach was designed to trigger an event within a cell of the model just once. In reality, often so-called 'seismic multiplets' are observed, i.e. seismic events that show very similar seismic signals. By analyzing the hypocenters of such events, one often observes the occurence of these events very close to each other, even sometimes at the same location in the medium. This is often interpreted as the cause of the so-called 'Kaiser effect' (Kaiser [1950]): It has been generally accepted that rocks, when stressed, emit acoustic emission (AE), e.g., microseismicity. The Kaiser effect can be defined as the absence of AE at stress levels below a previously applied maximum stress. The Kaiser effect for example has been studied at the German Continental Deep Drilling site (KTB) by Baisch and Harjes [2003]. In the proposed interpretation there it reads:

> *In this case the fluid pressure on the fracture plane reaches a plateau value and the ratio of $\tau/\sigma_{eff}$ ($\tau$ is the shear stress and $\sigma_{eff}$ the effective normal stress) gets 'frozen' as indicated towards later times in figure 3.36. As soon as the fluid pressure becomes stationary (time independent) on a fracture plane, seismicity on this fracture plane will stop since the amount of overcritical shear-stress (for the given fluid pressure) has already been released during previous seismic activity. The fracture 'remembers' the maximum fluid pressure it has previously experienced during the experiment. In material sciences such relaxation phenomena are known as the 'Kaiser effect' (Kaiser [1950]). Several observations made during KTB experiments indicate that relaxation phenomena play an important role in the spatio-temporal distribution of induced seismicity.*

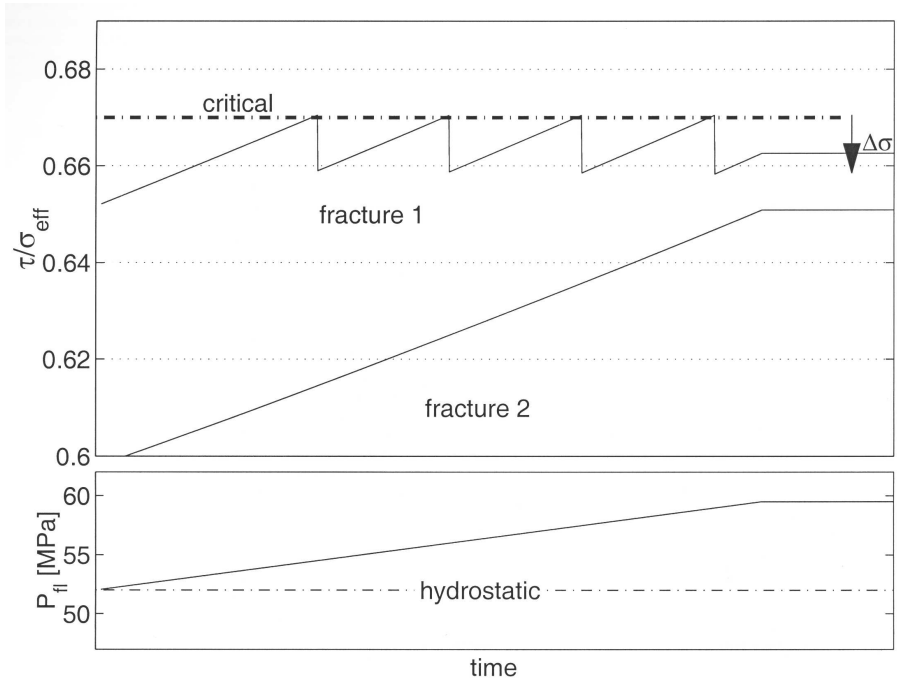


Figure 3.36: Simple sketch illustrating the repetition rate of a seismic multiplet. The ratio of shear to effective normal stress resolved on two different fracture planes is plotted against time under the assumption that fluid pressure on these fractures increases with time (bottom plot). If the coseismic stress drop $\Delta\sigma$ is small the same fracture will be ruptured several times while the other fracture plane remains inactive (from Baisch and Harjes [2003]).

The Kaiser effect influences the number of induced events and the spatio-temporal evolution. In order to study the effects on the estimations of hydraulic diffusivity using the SBRC approach, numerical modeling is extended to take into account the Kaiser effect. Two different approaches are realized as follows:

After distributing the criticality statistically in the medium, the numerical triggering process is started. For every time step and location, the amplitude of pressure perturbation is compared with the criticality in the corresponding cell as already proposed in chapter 3.1. Once the criticality value is exceeded, an event is triggered in the cell. Afterwards, so far the criticality was set to infinity in order to 'disable' the corresponding cell. No event could be triggered at this location for further time steps. In order to take into account the Kaiser effect, the criticality is not set to infinity now. In fact, it is just increased using two different criteria:

1. The first one is the possibility to increase the value according to the last criticality value within the cell. A percentage criterion is used to increase the criticality value e.g. by 10% of the last value. That means for example, a cell that previously contained a criticality of $C = 5$ is set to $C_{new}$=5.5 after being cracked for the first time. If a second event is triggered at this point, $C$ is set to $C_{new2}$=6.05 and so on. This procedure is called 'Kaiser effect based on cell value' (compare table A.2).

2. The second approach is based on the maximum criticality value of the whole medium $C_{max}$. If an elementary cell is triggered once, the previous value of criticality is increased due to a percentage criterion with regard to $C_{max}$. For example, if the criticality field is distributed between 0 and 10, a cell previously containing $C = 5$ is increased by 10% of $C_{max}$=10 and will be set to $C_{new}$=6 for the second triggering and after this to $C_{new2}$=7 and so on. This procedure is called 'Kaiser effect based on $C_{max}$' (compare with table A.2).

The result of numerical modeling of the Kaiser effect for one model is shown in figure 3.37. In figure 3.37a the simulation without Kaiser effect has been performed. The cloud of events after numerical triggering constists of 3769 events. The envelope fitting yields resonable agreement between numerical model and theoretical predictions. In figure 3.37b the same model is analyzed but now with a 15% increase of the maximum model criticality $C_{max}$=5. The cloud of events after modeling contains 3807 events, which is an increase of 38 events (+ 1%). Also in this case, the theoretical envelope matches the data quite well.

In figure 3.37c the modeling of the Kaiser effect based on the old cell value is shown. Here, the criticality of all cells once triggered is increased by 10% of the previous cell values. The cloud of events after modeling contains 40994 events, which corresponds to an increase of 37225 events or +987.7%. The seismic multiplets, i.e. events at different times at the same location, are clearly visible as horizontal structures in figure 3.37c. However, the theoretical envelope according to equation (2.6) fits 96% of all events. Therefore, one can conclude that the Kaiser effect as modeled here does not influence the estimations of the hydraulic parameters using the SBRC approach.

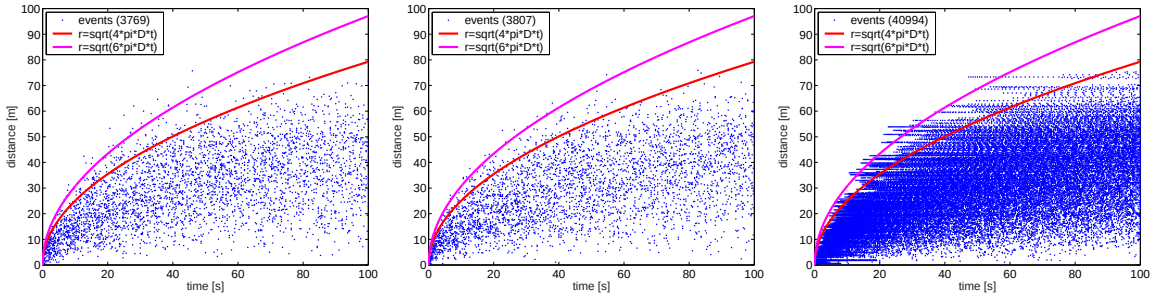


(a) (b) (c)

Figure 3.37: Simulation of the Kaiser effect for one numerical model (`m002`). a) Submodel no. 10 without kaiser effect. b) Submodel no. 25 with 15% of $C_{max}$, c) submodel 33 with 10% of previous cell values. For all models $C_{max}$=5 was used.

## 3.6 Conclusions of numerical modeling

Fluid injection induced microseismic activity is related to changes of pore pressure in pre-stressed rocks. Seismic monitoring of this microseismicity can be used to characterize rock hydraulic properties of geothermal or hydrocarbon reservoirs. Therefore, an approach called SBRC was recently proposed. The main hypothesis of the SBRC approach is that fluid-induced microseismicity is triggered due to a diffusive process of pore pressure relaxation in subcritically stressed rocks.

Using this hypothesis a simple numerical model is developed for simulating the space-time distribution of injection-induced microseismicity. These distributions depend on hydraulic properties and the statistics and spatial distributions of trigger criticality. The numerical simulations are applied to test the inversion approaches based on phase properties of diffusion waves of the pore pressure relaxation. The forward model results show time-distance distributions similar to observed microseismic clouds. This similarity supports the idea that the diffusive-like process of pore pressure relaxation is an important mechanism for triggering microearthquakes. It was shown that if the hypothesis is valid, than the inversion method based on equations (2.6) and (2.28 ) can be successfully used to reconstruct hydraulic properties of rocks from spatio-temporal evolutions of clouds of microseismic events on large spatial scales.

The numerical modeling approach presented here also yields the result, that triggering of microseismicity in rocks mainly depends on two physical fields: At first the distribution of hydraulic diffusivity in the medium and secondly the distribution of a criticality field of failure in terms of critical stresses. For all models analyzed it turns out that the distribution of these two fields influence the spatio-temporal distribution of microseismicity triggered in rocks. However, the first statistical moment of the criticality (i.e. distribution type) influences these distributions to a larger extend than the second statistical moment (i.e. spatial correlation of the criterion).

It was shown that the accuracy of the method presented to numerically solve the parabolic equation of diffusion is adequate to analyse the results in two and three dimensions. The eikonal-based equations of the SBRC algorithms were verified and it was shown, that the formal validity conditions of the SBRC are too restrictive. The modeling approach was illustrated in two dimensions from the model set-up, the distribution of criticality, the spatial correlation to the numerical triggering of events. The analysis confirms the SBRC algorithms even for the case of heterogeneous media.

The modeling in 3D was shown for homogeneous and anisotropic cases, accordingly. An envelope fitting criterion was developed and a slight modification of the SBRC algorithms was proposed. Different source functions as well as source geometries were studied according to observations from real hydraulic experiments. At last, it was found that a Kaiser effect, as it may be present in real rocks, does not influence the positive results of our estimations. Therefore, the numerical modeling approach presented in this chapter completely supports the SBRC approach. Main physical features of spatio-temporal distributions of microseismicity are observed as it is observable for real data. Additional observations permit the further development of the modeling and SBRC. Possibly, an extension of the model approach towards hydraulic fracturing or the combination with reservoir simulation software appears to be promising.